C910 chemical compound inhibits the traffiking of several bacterial AB toxins with cross-protection against influenza virus

Yu Wu, Nassim Mahtal, Eléa Paillares, Léa Swistak, Sara Sagadiev, Mridu Acharya, Caroline Demeret, Sylvie van Der Werf, Florence Guivel-Benhassine, Olivier Schwartz, et al.

iScience

CellPress
OPEN ACCESS

Article

C910 chemical compound inhibits the trafficking of several bacterial AB toxins with cross-protection against influenza virus

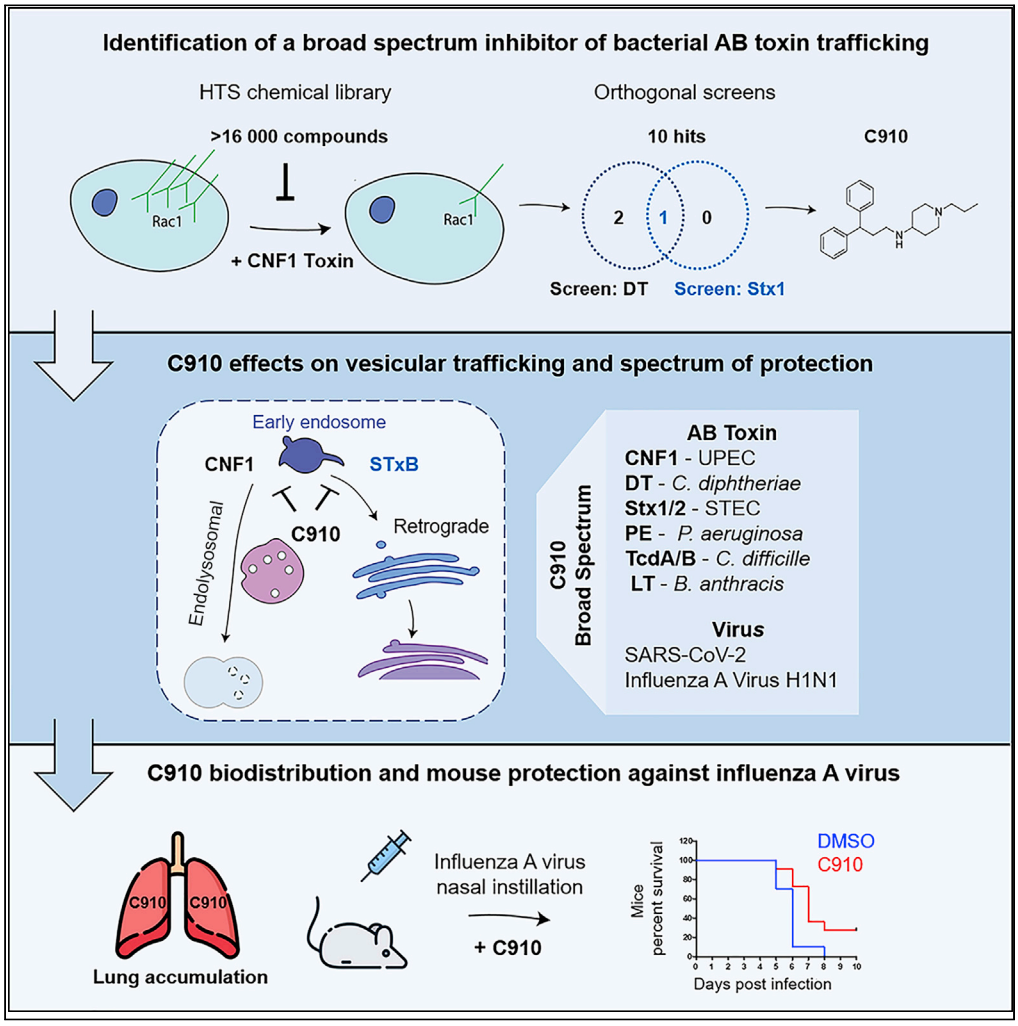

Yu Wu, Nassim Mahtal, Eléa Paillares, ..., Julien Barbier, Daniel Gillet, Emmanuel Lemichez

daniel.gillet@cea.fr (D.G.)
emmanuel.lemichez@pasteur.fr (E.L.)

Highlights

Screen for inhibitors disrupting bacterial AB toxins vesicular trafficking pathways

C910 affects EEA1/Rab5-positive early endosome morphology and sorting functions

C910 protects cells against eight AB toxins, SARS-CoV-2 and influenza A virus

C910 accumulates in lung tissues and protects mice against influenza A virus

Wu et al., iScience 25, 104537
July 15, 2022
https://doi.org/10.1016/j.isci.2022.104537

iScience

CellPress
OPEN ACCESS

Article

C910 chemical compound inhibits the traffiking of several bacterial AB toxins with cross-protection against influenza virus

Yu Wu,[1,12] Nassim Mahtal,[2,3,12] Eléa Paillares,[1,4] Léa Swistak,[1,4] Sara Sagadiev,[5] Mridu Acharya,[5] Caroline Demeret,[6] Sylvie Van Der Werf,[6] Florence Guivel-Benhassine,[7] Olivier Schwartz,[7] Serena Petracchini,[1,4] Amel Mettouchi,[1] Lucie Caramelle,[2] Pierre Couvineau,[2] Robert Thai,[2] Peggy Barbe,[2] Mathilde Keck,[2] Priscille Brodin,[8] Arnaud Machelart,[8] Valentin Sencio,[8] François Trottein,[8] Martin Sachse,[9] Gaëtan Chicanne,[10] Bernard Payrastre,[10] Florian Ville,[2,3] Victor Kreis,[2] Michel-Robert Popoff,[1] Ludger Johannes,[11] Jean-Christophe Cintrat,[3] Julien Barbier,[2] Daniel Gillet,[2,*] and Emmanuel Lemichez[1,13,*]

SUMMARY

The development of anti-infectives against a large range of AB-like toxin-producing bacteria includes the identification of compounds disrupting toxin transport through both the endolysosomal and retrograde pathways. Here, we performed a high-throughput screening of compounds blocking Rac1 proteasomal degradation triggered by the Cytotoxic Necrotizing Factor-1 (CNF1) toxin, which was followed by orthogonal screens against two toxins that hijack the endolysosomal (diphtheria toxin) or retrograde (Shiga-like toxin 1) pathways to intoxicate cells. This led to the identification of the molecule C910 that induces the enlargement of EEA1-positive early endosomes associated with sorting defects of CNF1 and Shiga toxins to their trafficking pathways. C910 protects cells against eight bacterial AB toxins and the CNF1-mediated pathogenic *Escherichia coli* invasion. Interestingly, C910 reduces influenza A H1N1 and SARS-CoV-2 viral infection *in vitro*. Moreover, parenteral administration of C910 to mice resulted in its accumulation in lung tissues and a reduction in lethal influenza infection.

INTRODUCTION

Host-directed anti-infective chemical compounds that interfere with intracellular membrane trafficking hold promise to alleviate pathophysiological manifestations triggered by bacterial toxins, thus shifting the host-pathogen balance in favor of the host (Kaufmann et al., 2018). Furthermore, these small molecules can be redirected against a wider number of infectious agents, notably numerous viruses that infect the vesicular compartments of cells (Gillespie et al., 2013; Gupta et al., 2017; Wu et al., 2017). The discovery of such molecules is currently a challenge in the expansion of available therapeutics against pathogens that produce toxins (Mühlen and Dersch, 2016).

Bacterial AB toxins are sophisticated nanomachines that bind and enter host cells thanks to their B-components in order to reach intracellular compartments where they find specific physicochemical conditions to translocate their enzymatic A-component into the cytosol. Selective disruption of vesicular trafficking can be leveraged to develop host-directed prophylactic and therapeutic measures against toxin-producing bacteria with broader applications in infectiology (Gillespie et al., 2013; Wu et al., 2017). To enter host cells, AB toxins exploit different endocytic pathways that converge toward the early endosomes from which they are dispatched into different vesicular pathways (Bassik et al., 2013; Moreau et al., 2011; Selyunin et al., 2017). AB toxins translocate their enzymatic part along the endolysosomal pathway or after retrograde transport to the ER which represent two hot spots of translocation (Ernst et al., 2017; Johannes and Romer, 2010). Early endosomes receive cargos, receptors, and pathogenic agents from the plasma membrane (Scott et al., 2014). They serve as an essential sorting station to reroute receptors and/or ligands to the cell surface through recycling endosomes, to the trans-Golgi network and ER through retrograde transport, or to late endosomes and then lysosomes for degradation. Each critical step along these vesicular pathways is specified by specialized membrane-associated protein complexes (Wandinger-Ness and

[1]Unité des Toxines Bactériennes, UMR CNRS 6047, Inserm U1306, Institut Pasteur, 25 rue du Dr Roux, 75724 Paris, France

[2]Université Paris-Saclay, CEA, INRAE, Département Médicaments et Technologies pour la Santé, SIMoS, 91191 Gif-sur-Yvette, France

[3]Université Paris-Saclay, CEA, INRAE, Département Médicaments et Technologies pour la Santé, SCBM, 91191 Gif-sur-Yvette, France

[4]Université Paris Cité, 75006 Paris, France

[5]Seattle Children's Research Institute, Jack R MacDonald Building, 1900 9th Avenue, Seattle, WA 98101, USA

[6]Unité Génétique Moléculaire des Virus à ARN, UMR 3569 CNRS, Université de Paris, Département de Virologie, Institut Pasteur, 28 rue du Dr Roux, 75724 Paris, France

[7]Unité virus et immunité, Département de Virologie, Institut Pasteur, 28 rue du Dr Roux, 75724 Paris, France

[8]Centre d'Infection et d'Immunité de Lille, Inserm U1019, CNRS UMR 9017, University of Lille, CHU Lille-Institut Pasteur de Lille, 59000 Lille, France

[9]Unité Technologie et service BioImagerie Ultrastructurale, Institut Pasteur, 28 rue du Dr Roux, 75724 Paris, France

[10]Inserm, UMR1297 and Université Toulouse III Paul Sabatier, I2MC, 31024 Toulouse, France

Continued

Zerial, 2014). Owing to their functions to sort receptors and ligands toward the endolysosomal or retrograde pathway, early endosomes represent potential targets of interest for the development of anti-infective displaying a large spectrum of actions against toxin-producing bacteria.

Cytotoxic Necrotizing Factor-1 (CNF1) toxin is produced by extraintestinal pathogenic *Escherichia coli* responsible for urinary tract infections, neonatal meningitis, and sepsis (Caprioli et al., 1984; Ho et al., 2018). The *cnf1* gene displays an estimated prevalence of 15% in *E. coli* sequence type (ST)131, which underwent an unprecedented global expansion in the last decade and represents a predominant multidrug-resistant (MDR) lineage of *E. coli* in extraintestinal infections (Petty et al., 2014). CNF1 binds to Lu/BCAM and 67-kDa laminin receptor (67LR) to enter cells by endocytosis and then traffics to late acidic endosomes. An acidic pH drives the translocation of the enzymatic A chain into the cytosol, where it deamidates a specific glutamine residue onto Rho proteins to abrogate their GTPase activity, leading to downstream signaling activation (Contamin et al., 2000; Flatau et al., 1997; Piteau et al., 2014; Schmidt et al., 1997). Inhibition of the GTPase activity of Rho proteins also sensitizes them to ubiquitin-mediated proteasomal degradation, leading to their cellular depletion in CNF1-intoxicated cells. The activation of Rho protein signaling by CNF1 endows pathogenic *E. coli* with an enhanced ability to invade host cells (Falzano et al., 1993; Visvikis et al., 2011).

Chemical compounds that interfere with the intracellular trafficking of bacterial toxins have shown efficacy against several infections caused by bacteria, viruses, and parasites *in vitro* and *in vivo*, as summarized in Tables S1 and S2. Known inhibitors act specifically on one of the two main endocytic pathways hijacked by toxins. Retro-2 acts specifically on the ER exit site component Sec16A, thereby compromising the interaction between the retrograde trafficking chaperones GPP130 and syntaxin-5 for proper transport of Shiga toxin to the ER (Forrester et al., 2020; Stechmann et al., 2010). Both EGA and ABMA exclusively affect the trafficking of AB toxins along the endolysosomal pathway by unidentified mechanisms (Gillespie et al., 2013; Wu et al., 2017). Host-directed anti-infectives targeting AB toxin sorting from early endosomes to their respective endolysosomal or retrograde pathways might be endowed with a broad spectrum of protection against toxins.

Here, we developed a high-throughput screening (HTS) pipeline that allowed the identification of a small chemical compound, C910, that protects host cells against eight different bacterial AB toxins. Moreover, the properties of C910 can be leveraged to confer protection against the flu caused by influenza A virus subtype H1N1 in mice and reduce SARS-CoV-2 cellular infection. Mechanistically, we provide evidence that C910 interferes with the sorting function of EEA1/Rab5-positive early endosomes.

RESULTS

Screening of chemicals targeting both the endolysosomal and retrograde transport of toxins

We developed a pipeline aimed at screening small chemical compounds that can protect host cells against a broad spectrum of bacterial AB toxins by hijacking either the endolysosomal (CNF1 and diphtheria toxin, DT) or the retrograde (Shiga-like toxin 1, Stx1) trafficking pathways (Figure 1A). We first performed HTS of 16,480 available chemical compounds from the ChemBridge DIVERSet library to determine their ability to protect primary human umbilical vein endothelial cells (HUVECs) from CNF1-induced cellular depletion of Rac1 (Figure 1B). We chose CNF1 for primary screening considering the interest in deciphering its endocytic pathway that does not involve clathrin and cholesterol-rich membrane domains (Contamin et al., 2000). The CNF1 toxin A domain exits the endolysosomal pathway at the level of late acidic compartments and deamidates small Rho GTPases, notably Rac1 (Flatau et al., 1997; Schmidt et al., 1997). The deamidated form of Rac1 is degraded by the ubiquitin–proteasome system, leading to progressive depletion of the cellular pool of Rac1 (Torrino et al., 2011). Thus, monitoring the intracellular pool of Rac1 allows for the screening of small chemical inhibitors of the cytotoxic effects of CNF1. Briefly, cells were treated with 10-nM CNF1 toxin for 6 h to achieve maximal depletion of the intracellular pool of Rac1 as monitored by quantitative immunofluorescence staining of Rac1 in cells (Figure 1B).

The threshold of chemically induced protection against CNF1-mediated depletion of Rac1 was set to 30% to identify robust candidate hits (Figure 1B). In total, 320 hits were cherry-picked and subjected to a second round of screening at 10 and 50 μM in triplicate. In sum, 66 compounds passed the second round of screening. These hits were subsequently reordered and freshly prepared for further validation and then filtered to eliminate pan-assay interference compounds (PAINS), i.e., unstable molecules, irreversible modifiers, or compounds that are

[11]Institut Curie, PSL Research University, Cellular and Chemical Biology unit, Endocytic Trafficking and Intracellular Delivery team, U1143 INSERM, UMR3666 CNRS, 26 rue d'Ulm, 75248 Paris, France

[12]These authors contributed equally

[13]Lead contact

*Correspondence: daniel.gillet@cea.fr (D.G.), emmanuel.lemichez@pasteur.fr (E.L.)

https://doi.org/10.1016/j.isci.2022.104537

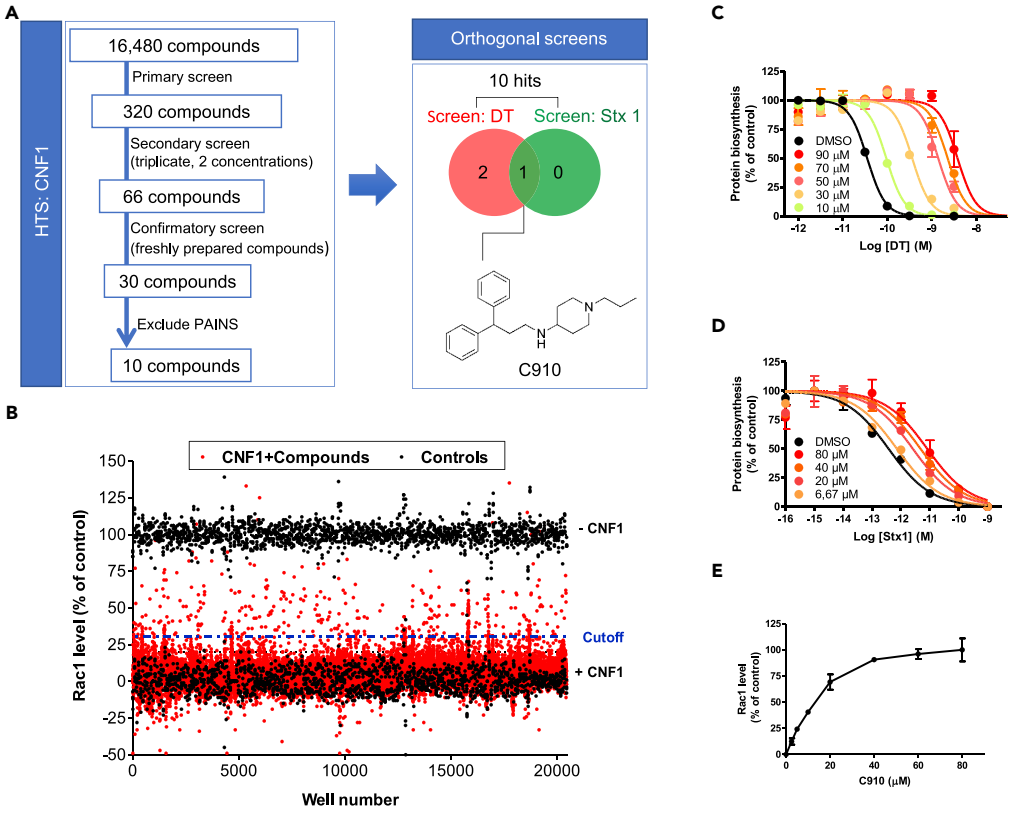

Figure 1. High-throughput screen of broad-spectrum antitoxin inhibitors

(A) General scheme and results of the screening pipeline developed to isolate small chemical compounds inhibiting the CNF1-mediated cell depletion of Rac1 followed by orthogonal screens with AB toxins hijacking the endolysosomal (DT) or retrograde (Stx1) pathways. Chemical structure of N-(3,3-diphenylpropyl)-1-propyl-4-piperidinamine, referred to as C910.

(B) ChemBridge library compounds were screened in HUVECs. Upper black dots represent positive controls (100% Rac1 signal in control HUVECs), whereas lower black dots correspond to Rac1 levels set to 0% in HUVECs exposed to 10-nM CNF1 for 6 h (negative controls). The red dots correspond to HUVECs incubated with chemicals in the presence of 10-nM CNF1 for 6 h. Cutoff (blue dashed line) was set to 30% of the Rac1 cellular signal. (C) and (D) graphs showing the dose-dependent protective effects conferred by C910 against protein biosynthesis inhibition at increasing concentrations of DT.

(C and D) Graphs showing the dose-dependent protective effects conferred by C910 against protein biosynthesis inhibition at increasing concentrations of DT (C) and Stx1 (D). HeLa cells were pretreated for 1 h in DMEM with C910 at the indicated concentrations (filled colored circles) or DMSO vehicle (black circles) prior to the addition of DT (C) or Stx1 (D) for 6 h and 18 h, respectively. Each point represents the mean of duplicates ± SD from one representative experiment (n = 3).

(E) Rac1 levels in CNF1-treated cells in the presence of increasing concentrations of C910. HUVECs were intoxicated with 10-nM CNF1 for 6 h in the absence or presence of C910 at the indicated concentrations. Each point represents the mean of duplicates ± SD from one representative experiment (n = 3).

See also Figure S1.

frequently active in other screens (Baell and Holloway, 2010). A total of 10 compounds were shortlisted as robust inhibitors of CNF1-mediated cellular Rac1 degradation. These compounds were subsequently analyzed for their protective actions against two bacterial toxins following either the endolysosomal or the retrograde pathway. These orthogonal screens were set to remove compounds with direct inhibitory action on the proteasomal degradation of Rac1 and identify compounds acting at the crossroad of the endolysosomal and retrograde pathways. For the orthogonal screening, we selected DT and Stx1 that rely on a well-studied transport route through the endolysosomal and retrograde pathways while targeting protein synthesis, unlike CNF1. Hence, DT was selected for the first orthogonal screen given its recognized capacity to translocate its A-domain from mature early endosomes (Papini et al., 1993; Ratts et al., 2003). The ADP-ribosyltransferase activity of DT catalyzes the post-translational modification of elongation factor-2 (EF-2), thereby blocking protein synthesis. The second orthogonal screen was conducted with Stx1, as it undergoes retrograde transport from early endosomes to

the Golgi before reaching the ER, where the A1 enzymatic subunit exits into the cytosol (Johannes and Romer, 2010; Sandvig et al., 1992). The *N*-adenine glycohydrolase activity of Stx1 cleaves an adenine of the 28S rRNA to inhibit protein biosynthesis. The cytotoxic effects induced by DT and Stx1 were quantified by measuring [^{14}C]-leucine incorporation into the neosynthesized cell proteins (Figures 1C and 1D). From the 10 lead compounds selected in the first screen, two molecules (see the STAR Methods section) were active against DT, and another was active against DT as well as Stx1. Taken collectively, this screening strategy allowed us to isolate one compound out of a total of 16,480 molecules, herein referred to as C910. The chemical structure of C910 can be divided into four parts (Figure 1A). As drawn, the western half bears two aromatic phenyl groups, whereas the eastern part contains a central amino group, a piperidine ring, and a terminal propyl chain.

We next calculated the half-maximal effective concentrations (EC_{50}s) for DT (60.1 μM), Stx1 (35.6 μM), and Stx2 (4.9 μM) (Figures 1C, 1D, and S1). We also determined that C910 inhibits the cytotoxic effects produced by 10-nM CNF1 with an IC_{50} = 11.3 μM (Figure 1E). Compound C910 thus displays EC_{50} values in the micromolar range, which is typical of nonoptimized hits found by HTS. We then evaluated the cytotoxicity of C910 in HUVECs and HeLa cells. We determined a CC_{50} value of approximately 100 μM for HUVECs that gave a selectivity index of ~9 for CNF1(Figure S1E). These data show that we identified a piperidinamine-derived compound that decreases host cell susceptibility to four different bacterial AB toxins by exploiting the endolysosomal (CNF1 and DT) or retrograde (Stx1 and Stx2) pathways.

C910 acts between the CNF1 cellular entry and Rho deamidation

C910 protects cells from CNF1, DT, and Stx, each of which has distinct catalytic activities and host cell receptors. This suggests that C910 acts on host cell components rather than on the particular enzymatic activities or receptor binding of the toxins. Consistent with this idea, we found that C910 did not affect the CNF1-mediated deamidation of RhoA *in vitro* (Figure S2A). Moreover, C910 did not affect the association of CNF1 with cell surface-exposed receptors nor its endocytosis. For this, CNF1 was chemically coupled to the fluorophore Cy3 (CNF1-Cy3) and incubated with cells at 4°C, allowing CNF1 to bind to its receptor on the cell membrane. Fluorescence-activated cell sorting (FACS) analysis showed that concentrations of C910 greater than its IC_{50} against CNF1 did not significantly influence the amount of CNF1-Cy3 bound to the cell membrane (Figure 2A). There was also no effect from C910 on the binding of the B-subunit of shiga toxin (STxB) to cell surface-exposed receptors (Figure S2B). Furthermore, C910 had no detectable effect on the internalization of CNF1 or STxB (Figures 2B and 2C).

The above data prompted us to examine the impact of C910 on the endolysosomal pathway. Here, we quantified the transport of fluid-phase endocytosed BSA to lysosomes by monitoring the acid-dependent protease-mediated dequenching of self-quenched red fluorescent DQ™ Red BSA (DQ-BSA) (Figures 2D and 2E). We verified that inhibiting endosomal acidification with the vacuolar H^+ ATPase (V-ATPase) inhibitor bafilomycin A1 (Baf A1) blocked DQ-BSA cleavage by acid-dependent proteases. When the chase was carried out for a short period of time (4 h), we observed a strong reduction in the signal from cleaved DQ-BSA in C910-treated cells compared with control vehicle-treated cells. However, C910 had no detectable effect on DQ-BSA cleavage in lysosomes after a longer reaction time. These data argue that C910 may target vesicular trafficking by lowering the flux of endolysosomal trafficking.

We next assessed the impact of C910 treatment on the acidic pH-dependent activity of cathepsin B and the density of the acidic compartments. First, C910 had no detectable effect on lysosomal cathepsin B activity measured both *in vitro* and in cells (Figures S3A and S3B). This argued for an absence of C910 interference with late endosome/lysosome acidification. The acidic compartment density was quantified by staining with LysoTracker Red DND-99, a membrane-permeable fluorescent dye that is protonated after the entry into acidic luminal compartments; this effect can be blocked by treating cells with the V-ATPase inhibitor Baf A1 (Pierzyńska-Mach et al., 2014). We did not measure variations in the percentage of LysoTracker-positive cells between the DMSO vehicle and C910 treatments (up to 40-μM C910) after 4 h of incubation, which was in contrast to the results after Baf A1 treatment (Figure 2F). Evidently, the defective endolysosomal trafficking flux is not related to pH variation in the acidic compartments.

C910 affects early endosome homeostasis, and CNF1 and Stx toxin sorting

To investigate the mechanism of action of C910, we analyzed the morphologies of the key vesicular compartments. This analysis was conducted after treating cells for a short period of time with C910 to avoid the cascade of effects on the interconnected endomembrane system. Immunolabeling of several protein

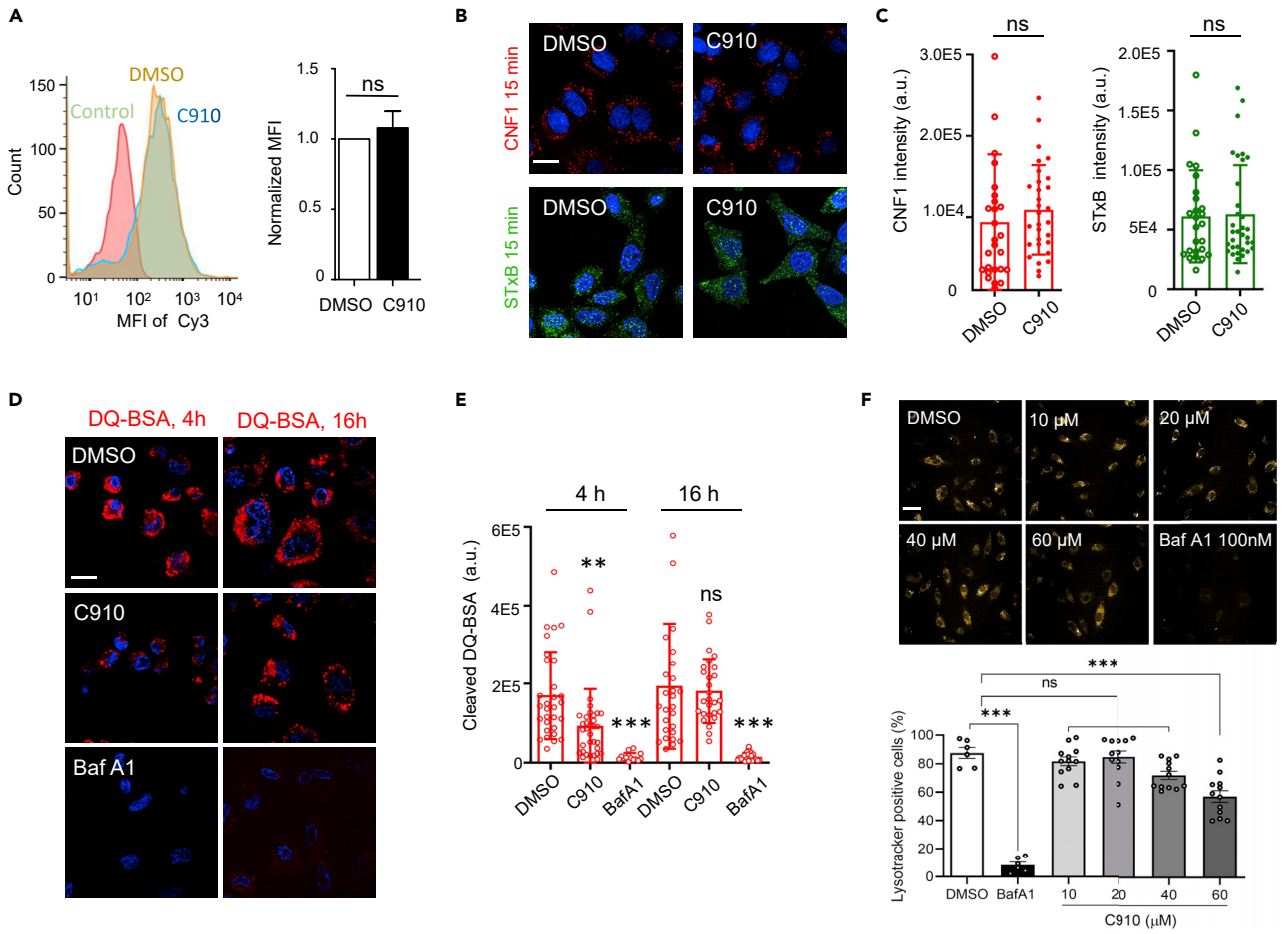

Figure 2. Absence of an impact from C910 on CNF1 and STxB entry into cells

(A) HUVECs were pretreated with DMSO vehicle or 40-µM C910 for 2 h and incubated with CNF1-Cy3 (1/500) on ice for 30 min in the presence of DMSO vehicle or 40-µM C910 before flow cytometry analysis. The signal from the control DMSO-treated cells was used as a background. The MFI (mean fluorescence intensity) of C910-treated cells was normalized to that of DMSO-treated cells. The histogram represents the mean ± SEM of three independent experiments. ns, not significant, paired two-tailed *t* test.

(B and C) Representative images (B) and quantification (C) showing that C910 does not affect the internalization of CNF1 or STxB. (B) Fifteen minutes of internalization of CNF1-Cy3 (red) in HUVECs and Alexa Fluor 488-STxB (green) in HeLa cells in the presence of DMSO vehicle or 40-µM C910. Nuclei were stained with DAPI (blue). Scale bar, 20 µm. (C) Quantification of the signal intensity of CNF1-Cy3 or Alexa Fluor 488-STxB associated with the cells. The mean values ±SD of the signal intensity measured for $n > 25$ cells per condition from one representative experiment are shown, $n = 3$. ns, not significant, unpaired *t* test.

(D) Representative images showing the signal intensity of cleaved DQ-BSA in HUVECs 4 h or 16 h after endocytosis under treatment with DMSO vehicle or 20-µM C910. Bafilomycin A1 (Baf A1) treatment was used as a positive control to inhibit acid pH-dependent endosomal proteases. Scale bar, 20 µm.

(E) Signal intensity quantification of cleaved DQ-BSA. The mean values ±SD of the signal intensity measured for n > 25 cells per condition from one representative experiment are shown, $n = 3$. ***p < 0.001, **p < 0.01, ns, not significant, one-way ANOVA.

(F) Representative images and percentage of LysoTracker-positive cells after treatment with DMSO vehicle, C910 (10, 20, 40, and 60 µM) or BafA1 (100 nM) for 4 h. Data show the mean ± SEM from three independent experiments, 12 repeats in total with $n > 800$ cells per condition. ***p < 0.001, ns, not significant, one-way ANOVA. Scale bar, 20 µm. See also Figure S2.

markers of cell compartments failed to detect a significant effect of C910 on the distribution and morphology of endolysosomal or retrograde pathway-related compartments with the exception of Rab5-positive early endosomes (Figure 3A). Indeed, compartments positive for Rab5 and early endosome antigen 1 (EEA1) appeared significantly enlarged and devoid of the late endosomal marker lysobisphosphatidic acid (LBPA) (Figures 3B and S3C). The extent of enlargement of EEA1-positive compartments increased as a function of incubation time and dose of C910 (Figures S4A and S4B). Transmission electron micrographs of endosomes from HUVECs incubated for 15 min with BSA-gold showed that the BSA-positive vacuoles had an electron-lucent lumen and few internal vesicles (Figure 3C). Moreover, we

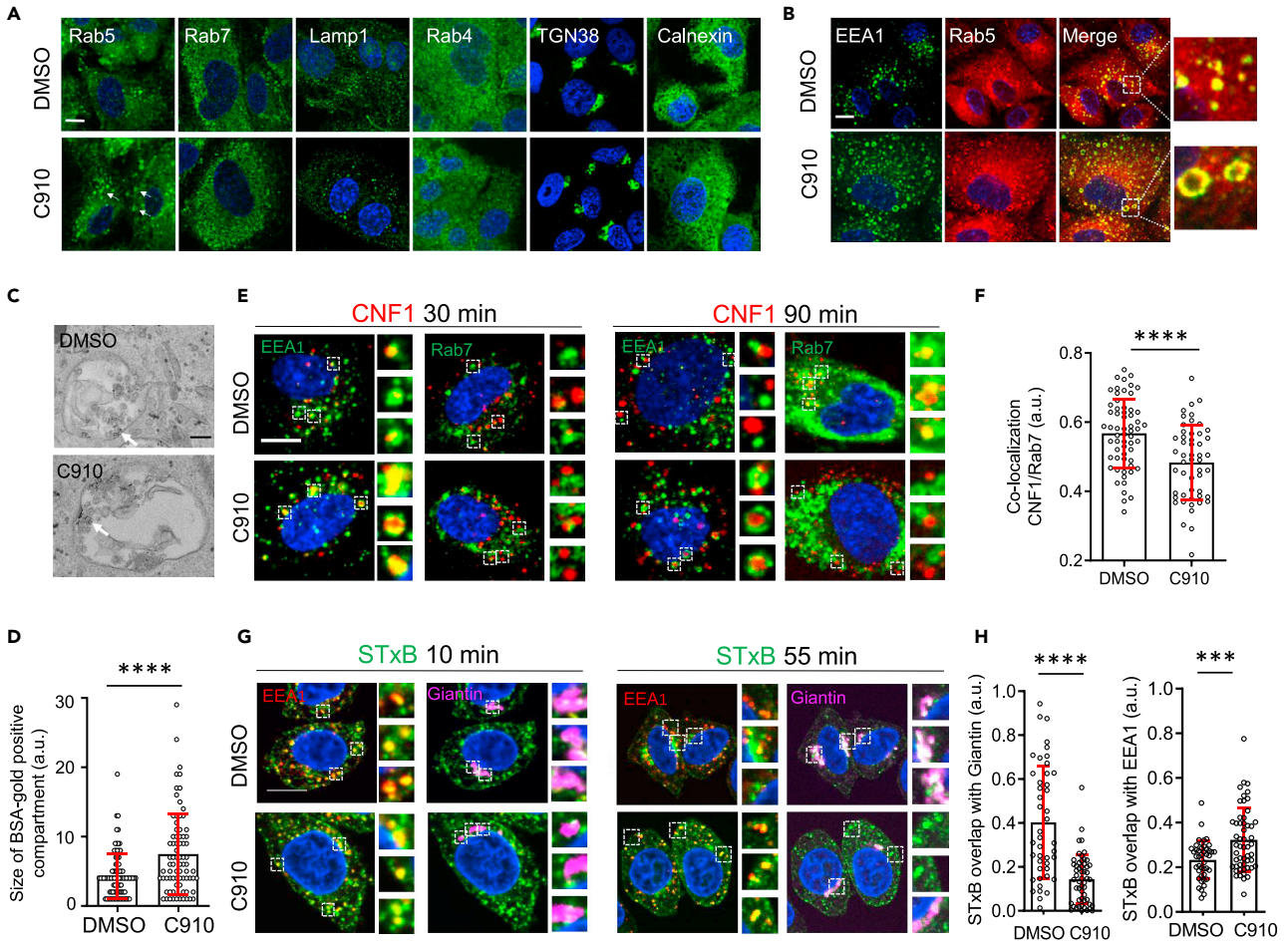

Figure 3. C910 alters the morphology and function of EEA1-positive early endosomes

(A and B) Immunofluorescence analysis showing the impact of C910 on early endosome morphology. A: HUVECs were treated with control DMSO vehicle or 40-μM C910 for 45 min and labeled for the indicated intracellular compartment markers. Nuclei were labeled with DAPI (blue). Scale bar, 10 μm. (B) Enlargement of the EEA1/Rab5-positive compartments in an HUVEC treated as in (A).

(C) Representative electron micrographs showing a BSA-gold-positive compartment after 15 min of endocytosis in a DMSO vehicle- or C910-treated HUVEC. White arrows indicate BSA-gold. Scale bar, 100 nm.

(D) Plot quantifying the sizes of the BSA-gold positive compartments from HUVECs as in (C). Each point represents an individual compartment, $n = 87$ (DMSO) and 77 (C910) from one representative experiment with the mean ± SD shown in red. ****$p < 0.0001$, unpaired two-tailed t test.

(E–H) Representative images and quantification of the distribution of CNF1-Cy3 in HUVECs (E–F) or Alexa Fluor 488-STxB (STxB) in HeLa cells (G and H) after two different times of endocytosis. Nuclei were labeled with DAPI (blue). Scale bar, 10 μm. (E) HUVECs were pretreated with DMSO vehicle or 40-μM C910 for 30 min followed by incubation with CNF1-Cy3 (red) for 30 min or 90 min in the presence of compound. Cells were labeled for EEA1 (green) or Rab7 (green). (F) Graph showing the Pearson's coefficient values of the cellular colocalization of the CNF1 and Rab7 signals for each cell (open circles), $n = 60$ (DMSO) and 51 (C910) with the mean ± SD in red. ****$p < 0.0001$, unpaired two-tailed t test. (G) HeLa cells were pretreated with DMSO vehicle or C910 40-μM before endocytosis of STxB (green) for 10 or 55 min in the presence of compound. Cells were then labeled for EEA1 (red) or Giantin (magenta). (H) Graphs showing the Mander's overlap coefficient values with the mean ± SD in red between the STxB and Giantin signals (left), as well as the STxB and EEA1 signals (right) for each cell (open circles), $n = 44$ (DMSO) and 53 (C910). Data from three independent experiments are expressed as arbitrary units (a.u.). ****$p < 0.0001$, ***$p < 0.001$, unpaired two-tailed t test. See also Figures S3 and S4.

quantified the significant increase in the size distribution of the BSA-gold-positive compartments in C910-treated cells compared with control (Figure 3D).

We then continued to define how cell treatment with C910 affects the trafficking of CNF1. After 30 min of intoxication, we observed a strong accumulation of CNF1-Cy3 in EEA1-positive endosomes (Figure 3E). Later, after 90 min of intoxication, we observed the preferential distribution of CNF1-Cy3 in Rab7-positive late endosomes. When cells were cotreated with C910 and CNF1-Cy3, we observed the accumulation of CNF1-Cy3 in the lumen of the enlarged EEA1-positive endosomes, which is associated with a deficit in

the transfer of CNF1-Cy3 in Rab7-positive late endosomes (Figures 3E and 3F). In line with the impact of C910 on the trafficking of CNF1 from early to late endosomes, we found that C910 treatment significantly increased the accumulation of Alexa Fluor 488 conjugated-STxB in EEA1-positive endosomes (Figures 3G and 3H). This was at the expense of STxB transfer to the Golgi apparatus, as determined by Giantin immunostaining (Figures 3G and 3H). Thus, C910 affects the trafficking of CNF1 and fluid-phase endocytosed BSA through the endolysosomal pathway as well as the trafficking of STxB from early endosomes to the Golgi network, thereby protecting host cells against CNF1 and Stx toxins.

We concluded that C910 disrupts the vesicular trafficking at the level of the early endosomes.

Extended spectrum of protection against bacterial AB-like toxins

We next sought to characterize the antitoxin spectrum of C910 by studying a collection of AB toxins that transit through early endosomes to intoxicate cells. Exotoxin A (PE) from *Pseudomonas aeruginosa*, shares with DT and Stx the capacity to block protein biosynthesis. PE exploits the intertwined endolysosomal and retrograde pathways (Alami et al., 1998; Kounnas et al., 1992) to reach the ER for translocation into the cytosol (Michalska and Wolf, 2015; Moreau et al., 2011). Cells were intoxicated with increasing doses of PE in the presence of 5–20-μM C910 or treated with vehicle (DMSO), and an EC_{50} value of 12.6 μM was established (Figure 4A and Figure S1D). We next pursued the study of AB toxins that translocate their A-enzymatic components through a pore formed by B-subunit oligomers at acidic pH. Anthrax toxin from *Bacillus anthracis* is composed of protective antigen (PA), lethal factor (LF), and edema factor (EF) (Collier and Young, 2003). The 63-kDa mature form of PA undergoes hepta- or octamerization at the cell surface in association with receptors, leading to toxin-receptor endocytosis (Bradley et al., 2001; Scobie et al., 2003; Wei et al., 2006), whereas LF and EF translocate through oligomerized PA (Collier and Young, 2003). HUVECs were intoxicated with two different concentrations of lethal toxin (LT: PA + LF), both of which are sufficient to induce complete cleavage of MEK2, the substrate of LF, within 2 and 4 h (Figure 4B). We found that the addition of 40-μM C910 markedly delayed the kinetics of MEK2 cleavage by protection factors between 2.2 (LT) < p < 2.5 ($LT_{1/10}$) (Figures 4B and 4C). This result demonstrates the protection conferred by C910 to host cells intoxicated with LT from *B. anthracis* over time. We then tested the effect of C910 on the large clostridial glucosylating toxins (LCGTs) TcdA and TcdB from *Clostridium difficile* (Papatheodorou et al., 2018). These toxins hijack different host receptors to enter cells via endocytosis and translocate from acidified endosomes (Aktories et al., 2017; Chen et al., 2021; Tao et al., 2019). The internalization of LCGTs occurs via a dynamin-dependent process that largely involves clathrin. LCGTs glucosylate a threonine residue in the effector binding loop of Rho GTPases to short circuit the signaling cascades that control the actin cytoskeleton. Consequently, this produces cell rounding. Highly sensitive Vero cells were intoxicated with eight cytotoxic units of TcdA or TcdB, conditions that were set to reach 100% cell rounding after 8 h of intoxication. Under these conditions, cotreatment of cells with 5-μM C910 markedly reduced the percentages of cells rounding (Figure 4D). The extent of protection conferred by C910 on LCGT cytotoxicity was quantified by anti-Rac1 immunoblotting (Figure 4E). This assay is based on the observation that glucosylation of threonine-35 of Rac1 blocks its recognition by the anti-Rac1 [clone 102]-monoclonal antibody (Halabi-Cabezon et al., 2008). These data allowed direct visualization of the dose-dependent inhibition conferred by C910 on the LCGT-driven post-translational modification of Rac1, which reached a maximum at 20 μM (Figure 4E).

The protective effects displayed by C910 treatment on cells intoxicated with eight different bacterial AB toxins argue for the broad action of C910 on the early stages of intracellular trafficking, before bifurcation between the endolysosomal and retrograde pathways.

C910 inhibits CNF1-mediated cell invasion by uropathogenic *E. coli* (UPEC)

We next examined whether C910 may have notable applications in infectiology by protecting cells against the CNF1-mediated internalization of UPEC. Invasion of epithelial and endothelial cells by UPEC leads to recurrent and severe forms of infection (Klein and Hultgren, 2020). The efficiency of cell invasion was quantified by treating cells with a defined amount of recombinant CNF1 toxin and infecting them with a strain of UPEC, which lacks both the *cnf1* and alpha-hemolysin *hlyA* encoding genes that would otherwise lyse the host cells *in vitro*. Extracellular bacteria were then killed by treating the cell culture with nonpermeable gentamicin, and viable intracellular bacteria were enumerated by measuring the number of colony-forming units on agar plates following cell lysis (Doye et al., 2002). We first verified that C910 at 15 μM, close to its EC_{50} determined for CNF1, had no impact on the bacterial growth kinetics (data not shown). Figure 5A shows that neither C910 nor CNF1 affected the binding of the bacteria to the cells. Figure 5B shows that the bacteria could invade cells and escape from the gentamicin treatment only in the presence of CNF1.

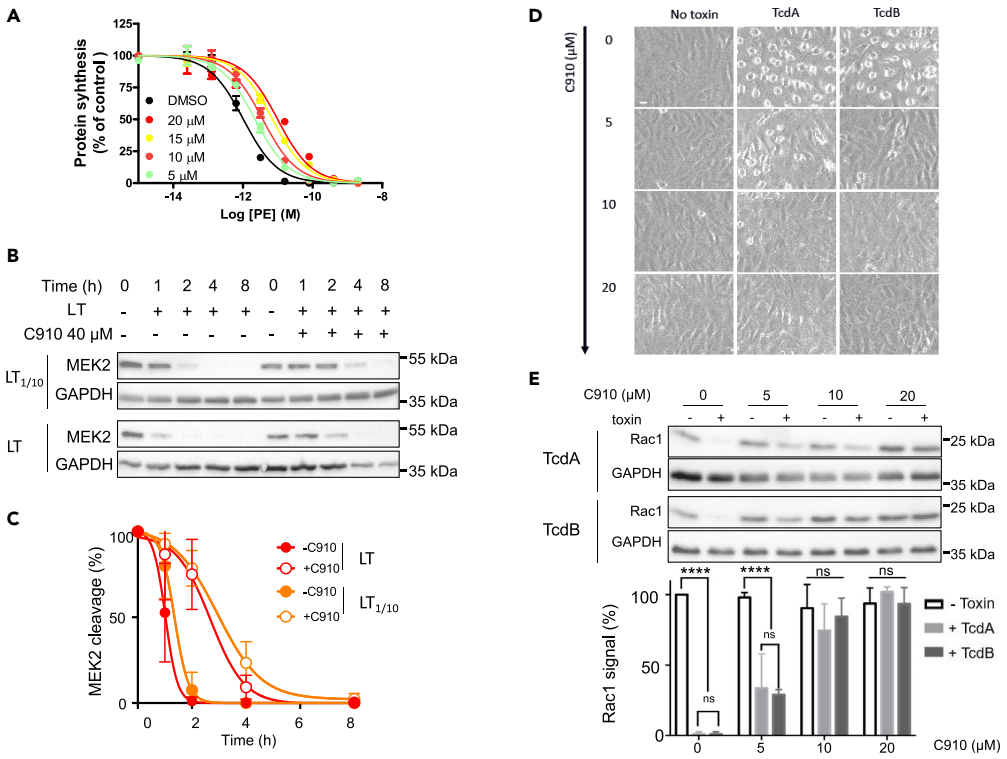

Figure 4. Extended spectrum of protection conferred by C910 against AB toxins

(A) Dose-dependent protective effect conferred by C910 against protein synthesis inhibition by PE from *P. aeruginosa*. L929 cells were pretreated for 1 h with control DMSO vehicle (black circles) or C910 at the indicated concentrations (filled colored circles) before the addition of PE for 18 h. Each point represents the mean of duplicates ±SD from one representative experiment (n = 3). See also Figure S1D.

(B) Immunoblots showing the kinetics of MEK2 cleavage at two concentrations of LT (PA: 0.3 µg/mL, LF: 0.1 µg/mL (LT) or diluted 1/10 ($LT_{1/10}$) in the absence or presence of 40-µM C910. Anti-GAPDH immunoblots were used as loading control. The blots are representative of four independent experiments.

(C) Non-linear regression curves of the normalized MEK2 levels as a function of time (h) ($R^2 > 0.9$) under the conditions described in (B). The curves show the percentages of the MEK2 signal as a function of time in HUVECs intoxicated with LT (red circles) or $LT_{1/10}$ (orange circles) in the presence of DMSO vehicle (filed circles) or 40-µM C910 (open circles). Each point represents the mean ± SD from four independent experiments.

(D) Vero cells intoxicated with eight cytotoxic units (cu) of TcdA or TcdB for 8 h in the presence of DMSO vehicle or C910 at the indicated concentrations. Scale bar, 10 µm.

(E) Anti-Rac1 immunoblots showing the non-glucosylated form of Rac1 in Vero cells treated as in (D). The histogram corresponds to the Rac1 signals normalized to GAPDH and set to 100% for the control conditions. Data are expressed as the mean ± SD, n = 3 independent experiments. Two-way ANOVA with Tukey's multiple comparison test was used to compare toxin-treated cells with non-intoxicated controls in the presence of C910 at different concentrations, ****$p < 0.0001$; ns, not significant.

However, cotreatment with C910 abrogated the positive effect of CNF1 on cell invasion. These results highlight the importance of CNF1 for the invasion of host cells by UPEC. Infected cells were also monitored for the CNF1-mediated depletion of Rac1, further showing the protective action of C910 (Figure 5C). In contrast, we found that C910 did not confer protection during the Rac1-dependent invasion of cells by *Salmonella typhimurium* (Figures 5D, 5E, and 5F). Cell-bound *S. typhimurium* directly injects Cdc42/Rac1-activating effectors through type-3 secretion system (T3SS)-1, thereby bypassing the endocytosis and intracellular trafficking steps required for AB toxin action, including CNF1 (Hardt et al., 1998). Collectively, these data show that C910 dramatically diminishes an essential step of UPEC infection by blunting the cytotoxic effects of CNF1 and has no effect on Rac1-driven large-scale membrane deformations triggered by *Salmonella* to induce macropinocytosis into host cells.

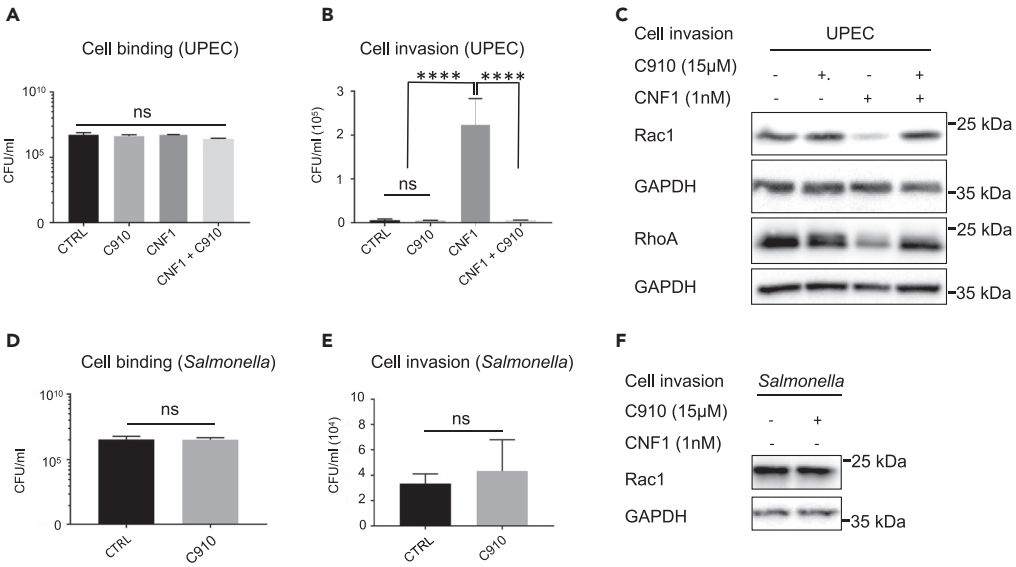

Figure 5. C910 protects cells from UPEC invasion mediated by CNF1

(A–F) Measurements of cell invasion by uropathogenic *E. coli* UTI89Δ*hlyA*Δ*cnf1* (UPEC) (A, B, and C) and *Salmonella enterica* serovar Typhimurium SL1344 (*Salmonella*) (D, E, and F). HUVECs were preincubated for 30 min with DMSO vehicle or 15-μM C910 before UPEC infection for 2.5 h in the absence or presence of 1-nM CNF1. HUVECs were preincubated for 3 h with DMSO vehicle or 15-μM C910 before infection with *Salmonella* in the absence or presence of C910 for 1 h. Graphs show the number of viable bacteria associated with the cells (A and D) or viable intracellular bacteria resistant to gentamicin treatment (B and E). Values correspond to colony-forming units (CFU)/mL, presented as the mean ± SEM from three independent experiments. One-way ANOVA was performed overall ($p < 0.0001$) with Tukey's multiple comparison test to compare the treated conditions in (A) and (B), ****$p < 0.0001$; ns, not significant. Data in (D) and (E) were analyzed by an unpaired two-tailed *t* test, ns, not significant. (C) Immunoblots of anti-Rac1 and anti-RhoA showing that C910 blocked CNF1-mediated Rac1 and RhoA depletion during cell infection by UPEC, as described in (B). (F) Immunoblot of anti-Rac1 showing that C910 and/or Salmonella infection, as described in (E), did not affect Rac1 cellular levels. Anti-GAPDH was used as a loading control.

C910 inhibits cell infection by influenza A virus H1N1 and SARS-CoV-2

Numerous viruses, as bacterial AB toxins, exploit the intracellular trafficking to infect host cells. Thus, to what extent can C910 be leveraged to block cell infection by viruses responsible for pandemics? Past flu pandemics include among others the devastating Spanish flu (>50 million deaths worldwide) and the more recent 2009H1N1 pandemic, both owing to influenza A viruses (IAV). More recently, the emergence of SARS-CoV-2, the etiologic agent of coronavirus disease (COVID) 2019, resulted in a global pandemic affecting more than one billion people. These repeated pandemic episodes of severe pneumonia of viral origin call for the development of broad anti-infective strategies against viral pathogens.

To invade host cells, several viruses including IAV and SARS-CoV-2 share with AB toxins the need for the physicochemical conditions and host proteases found inside endosomes. The well-defined IAV trafficking in host-cell compartments shows that viral particles enter cells by multiple endocytic mechanisms and traffic through EEA1-positive early endosomes before the release of genetic material into the cytosol from late endocytic compartments (Dou et al., 2018; Sieczkarski and Whittaker, 2003). The infection of cells by SARS-CoV-2 involves the virus binding to the angiotensin-converting enzyme 2 (ACE2) receptor (Zhou et al., 2020) and the processing of the spike glycoprotein by host proteases at the plasma membrane and in late endosomes for membrane fusion (Mitra, 2020). Processing of the spike protein expressed at the plasma membrane of infected cells by the serine protease TMPRSS2 also facilitates cell–cell fusion and syncytia formation (Buchrieser et al., 2020).

We first examined the effect of C910 on a single IAV infectious cycle. A549 human pulmonary epithelial cells pretreated with C910 or vehicle alone were infected with a reporter $H1N1_{WSN}$ virus expressing the mCitrine fluorescent protein. The expression of mCitrine from this reporter virus reflects viral genome replication

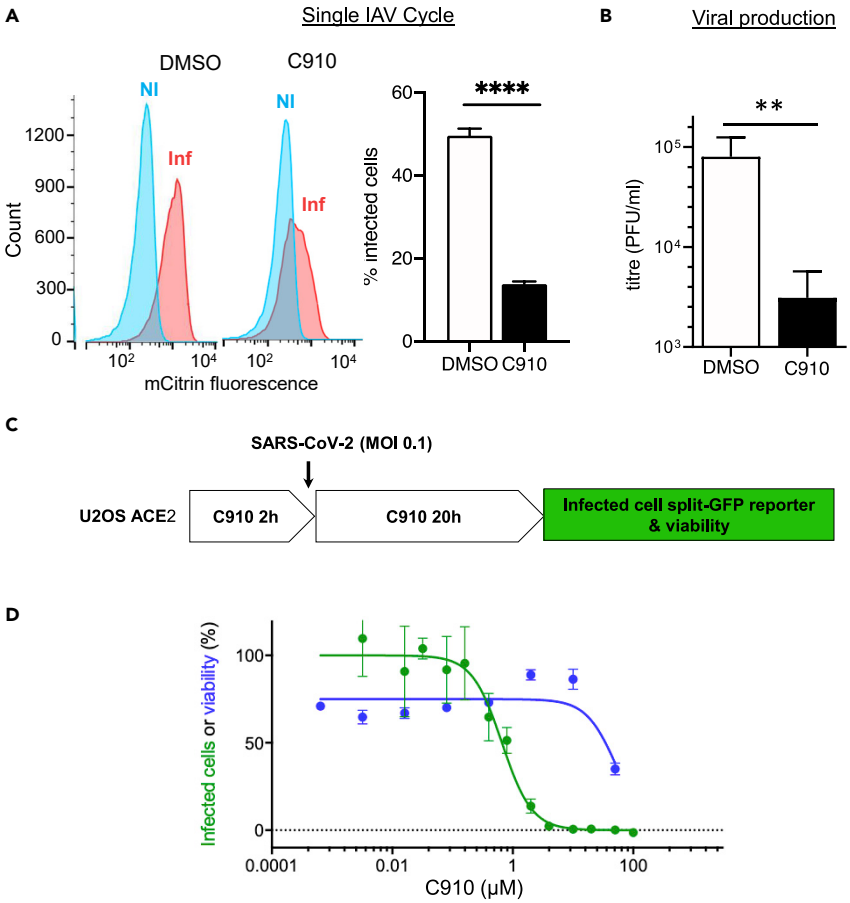

Figure 6. C910 inhibits IAV H1N1 and SARS-CoV-2 cellular infection

(A) C910 inhibits a single H1N1 IAV cycle. A549 cells were pretreated with DMSO vehicle or C910 (30 µM) for 1 h at 37°C before infection with the $H1N1_{WSN}$ mCitrin reporter virus at an MOI of 5. At 6 h post-infection, the cells were analyzed by flow cytometry. mCitrin fluorescence (left) is shown for non-infected (NI) or infected cells (Inf). The histogram (right) represents the percentage of infected cells, which was calculated as the mean ± SEM of six replicates from one representative experiment (n = 2). ****p < 0.0001, unpaired two-tailed t test.

(B) C910 inhibits H1N1 IAV virion production. A549 cells were infected with $H1N1_{pdm09}$ at an MOI of 0.001 in the presence of DMSO vehicle or 30-µM C910. Viral production was titrated at 24 h post-infection from the cell supernatant with a plaque-forming assay. The histogram represents the mean ± SD of three replicates in one representative experiment (n = 2). **p = 0.005, unpaired two-tailed t test.

(C) Schematic protocol of SARS-CoV-2 infection. U2OS-ACE2 GFP1-10 and GFP11 cells were preincubated with C910 for 2 h, and then SARS-CoV-2 at MOI = 0.1 was added for 20 h. The relative infection efficiency was calculated as the ratio between the GFP area and the total number of cells stained with DAPI.

(D) Data are shown as the mean ± SD from duplicate wells, one representative experiment (n = 3).

(Biquand et al., 2017). We measured the cell infection efficiency by flow cytometry after the short time period of 6 h and found that C910 treatment reduced the percentage of infected cells by 3.6-fold, from 49.64 ± 4.12% (DMSO) to 13.83 ± 1.58% (C910) (Figure 6A, right panel). We then monitored the effect of C910 on multiple cycles of infection. After a longer infection, C910 decreased the viral titer by 25.8-fold, thereby demonstrating the strong inhibitory action of C910 on IAV cell infection (Figure 6B).

As with many viruses, SARS-CoV-2 relies on the components of endocytic pathways to infect cells (Gordon et al., 2020; Riva et al., 2020). This encompasses the activity of PIKfyve kinase, which resides predominantly in early endosomes to regulate endomembrane homeostasis and is also the specific target of apilimod, a compound that blocks SARS-CoV-2 replication (Riva et al., 2020). We tested the effect of C910 in a cellular model of SARS-CoV-2 infection. Here, a mixed population of U2OS cells stably expressing ACE2 (U2OS-ACE2) and a GFP-split complementation system in which two cells separately express half of the reporter

protein (GFP1-10 or GFP11) and produce GFP only upon intercellular fusion (Buchrieser et al., 2020). The extent of the GFP-positive area generated by cell fusion is a function of the viral inoculum, thereby providing a quantitative assessment of viral infection. U2OS-ACE2 cells were preincubated with C910 before viral exposure, and viral infection was investigated after 20 h (Figure 6C). Compound C910 inhibited SARS-CoV-2 infection with an IC_{50} of 0.74 $\pm$ 0.07 μM (Figure 6D). Collectively, these results widen the anti-infective spectrum of C910 against two RNA viruses that proceed through the endolysosomal pathway.

Both C910 and the PIKfyve inhibitor apilimod induced the enlargement of EEA1-positive early endosomes (Figure S5A) (Nelson et al., 2017). This result suggested that C910 could possibly act on PIKfyve. Nevertheless, we found that apilimod had no protective effect on the CNF1-mediated degradation of Rac1 (Figure S5B), and conversely, C910 did not inhibit PIKfyve kinase activity *in vitro* (Figure S5C). Interestingly, C910 displays broad anti-infective properties through a molecular mechanism that is different from that of apilimod, although both compounds induce the enlargement of Rab5/EEA1-positive endosomes.

C910 accumulates in lung tissues and protects mice against lethal influenza

The pharmacokinetic (PK) parameters and pulmonary biodistribution of C910 following intraperitoneal administration to mice were first defined. Figure S6A shows that at a dose of 10 mg/kg, the plasmatic concentration of C910 reached a maximum (C_{max}) of 164 $\pm$ 33 nM at 15 min, followed by a sharp decline to a prolonged plateau of approximately 25 nM for at least 24 h. C910 displays a half-life ($T_{1/2}$) of 28.5 $\pm$ 4.3 h in plasma, indicating long exposure and slow elimination from the organism. Following a single intraperitoneal injection of C910 at 20 mg/kg/mouse, we found 7–7.8 μg of C910 in whole lungs 1 h post-injection, and 6.7– 7.4 μg 4 h post-injection. This corresponds to lung tissue concentrations of 100–116 μM after 1 h and 61–110 μM after 4 h. We next investigated the effect of intraperitoneal injection of 20 mg/kg C910 on major blood chemistry parameters, e.g., markers of hepatic, pancreatic, renal, and cardiomuscular functions, using an approved field-portable clinical device. No toxicity and no statistically significant differences were found between vehicle control C910-treated and vehicle control animals at 24 h post-administration (Figure S6B). Thus, despite low plasmatic concentrations, C910 accumulates in lung tissues at concentrations around 100 μM for several hours after challenging mice with 20 mg/kg with no detectable toxic effects. These concentrations are about three-fold the effective inhibitory concentration found *in vitro* against IAV H1N1.

We then proceeded to proof-of-concept experiments starting in a prophylactic setting. C57BL/6 mice were intraperitoneally injected with 20 mg/kg C910 and then challenged with the infectious IAV H1N1 strain PR/8 (Figure 7A). At a low dose of the virus that is known to induce weight loss and subsequent mortality, we recorded complete protection in C910-treated mice, whereas the vehicle control-treated animals had to be euthanized during the course of infection owing to excessive weight loss or serious symptoms (Figures S6C and S6D). When the animals were challenged with a higher dose of virus in the same experimental setting, we recorded that C910 treatment improved mouse survival and reduced mouse weight loss (Figures 7B and 7C). Indeed, half of the C910-treated mice survived, whereas all of the vehicle-treated mice had to be euthanized starting on Day 5. In a therapeutic setting (Figure 7D), repeated injections of C910 starting 24 h after viral infection significantly increased mouse survival and attenuated weight loss (Figures 7E and 7F). Taken collectively, these findings show a beneficial effect of C910 against IAV infection in mice, which can be attributed to the accumulation of C910 in lung tissues at an effective dose as defined *in vitro*.

We conclude that C910 displays an extended protection spectrum against two viruses responsible for severe pneumonia in addition to eight bacterial AB toxins. In addition, a proof of concept of *in vivo* efficacy against a viral infection was established in mice.

DISCUSSION

We isolated by HTS a piperidinamine-derived chemical compound that protects host cells against a wide spectrum of structurally unrelated AB toxins that hijack either the endolysosomal or retrograde trafficking pathways to intoxicate cells. Mechanistically, we established that C910 impacts the size of Rab5/EEA1-positive endosomes and affects the routing of CNF1 and STxB from early endosomes to late endosomes and to the trans-Golgi network (TGN), respectively. We leveraged the properties of C910 to protect cells against infection by a CNF1-producing strain of UPEC, IAV H1N1, and SARS-CoV-2 and mice against IAV H1N1.

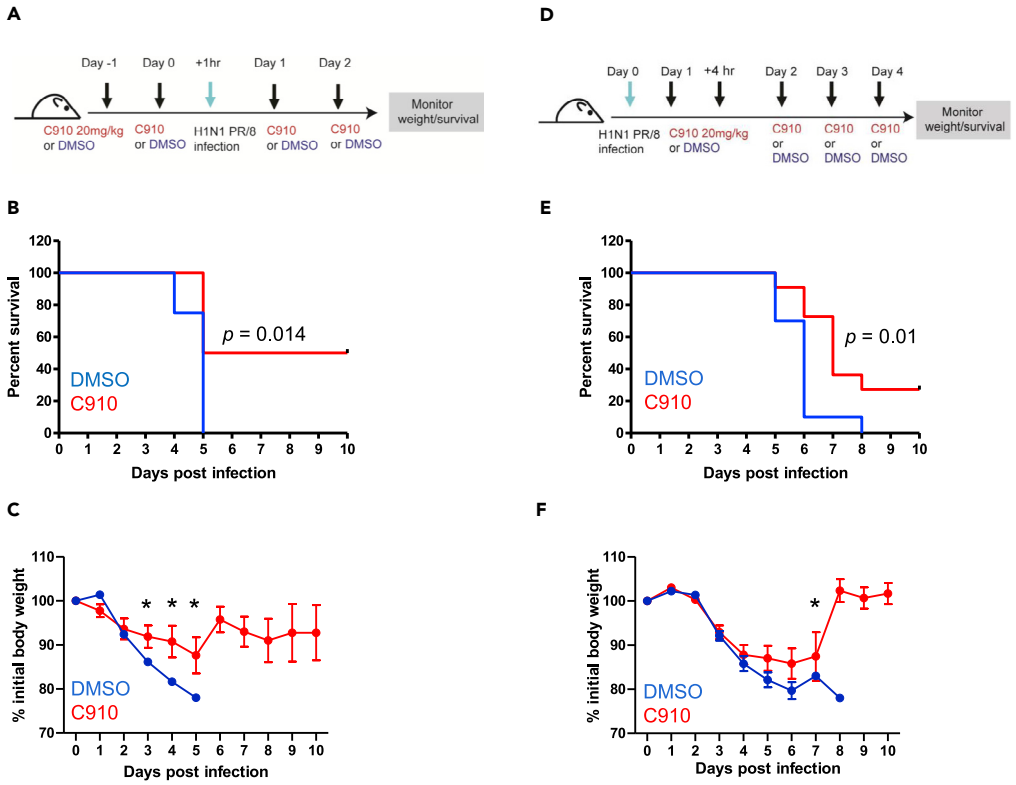

Figure 7. C910 protects mice against IAV H1N1 infection

(A and D) Timeline of the procedure.

(B and C) Survival curves (B) and weight loss (C) following intranasal infection with PR/8, as described in (A) for mice treated with control DMSO vehicle (n = 8) or C910 (n = 8).

(E and F) Survival curves (E) and weight loss (F) following intranasal infection with PR/8 as described in (D) for mice treated with control DMSO vehicle (n = 10) or C910 (n = 11). The Mantel–Cox test was performed to compare the survival curves between the groups injected with DMSO or C910. Weight loss data are shown as the mean ± SEM, *p < 0.05, multiple t test. See also Figure S6.

We carried out stringent orthogonal screens of a chemical library against CNF1, DT, and Stx1, which nonetheless led to the identification of a compound targeting the two major vesicular trafficking pathways hijacked by AB-like toxins compared with other antitoxin chemicals identified to date (Table S2). As summarized in Table S2, the previously isolated chemical compounds display specific actions on a large panel of toxins that traffic through one or the other of these two major pathways, as opposed to the broader spectrum of action of C910. These compounds comprise EGA as well as ABMA and Retro-2, which were selected against the lethal toxin from *B. anthracis* and the plant toxin ricin (Gillespie et al., 2013; Stechmann et al., 2010; Wu et al., 2017). C910 is able to inhibit Stx1/2, which are excluded from the antitoxin spectra of ABMA and EGA. Moreover, Retro-2 is devoid of a protective effect against endolysosomal-based toxins, e.g., DT and CNF1 (unpublished data).

The importance of these chemical modulators of vesicular trafficking in deciphering the key steps of these pathways and toxin mechanisms of action perfectly illustrates the cross-feeding between the disciplines of cell biology and infectiology (Forrester et al., 2020; Sandvig et al., 1991; Selyunin et al., 2021). Notably, these different compounds have been used as tools to discern the different physicochemical requirements of AB toxins. For example, CNFy and CNF3 showed distinctive sensitivity to EGA but similar dose-response profiles to ABMA, indicating differential endosomal escape of the two highly homologous toxins (Haywood et al., 2021). Similarly, tamoxifen was identified in a drug repurposing screen to block the fusion of late endosomes with lysosomes with consequences on the dynamics of retromer cycling on early endosomes, leading to the impaired sorting of Stx1 and Stx2 toxins from early endosomes to the Golgi network (Selyunin et al., 2019, 2021).

The efficacy of C910 varies according to the investigated toxin or pathogen. The EC_{50} values varied from ~5 to ~60 μM for the examined bacterial toxins and were as low as <1 μM for SARS-CoV-2. The high efficacy of vesicular trafficking-disrupting drugs against viruses compared with AB toxins is comparable to that of ABMA, with EC_{50} values of ~60–90 μM against several bacterial toxins, ~ 4 μM against ricin toxin and Ebola virus, and ~10 μM against rabies virus and dengue virus 4 (Wu et al., 2017). The diphtheria toxin that translocates from mature early endosomes displayed the highest EC_{50} of 60.1 μM compared with the other AB toxins studied. This may reflect differences in the mechanisms of translocations of these toxins that are differentially affected by the effect of C910 on the dynamics of endolysosomal trafficking. In contrast, toxins that have to reach late endosomes for translocation, such as CNF1 and LCGTs from *C. difficile*, or be processed there, such as PE from *P. aeruginosa*, all display similar susceptibilities to C910. Thus, C910, by interfering with the size of early endosomes and their sorting function toward the endolysosomal and retrograde pathways, represents a new compound to study vesicular trafficking dynamics and differences in translocation mechanisms among bacterial toxins. Also, the common denominator of the antitoxin and anti-viral effects of C910 may help to conceive new host-directed broad-spectrum anti-infective drugs.

Herein, we endow C910 with a function to disrupt vesicular trafficking in early endosomes. Indeed, C910 does not affect the binding and endocytosis of CNF1 and Stx1 although it induces the enlargement of Rab5/EEA1-positive early endosomes and affects the sorting of CNF1 and STxB to late endosomes and the Golgi network, respectively. C910 affects the morphology of early endosomes in this time window of treatment without inducing detectable changes in the subcellular distribution and morphology of the other organelles studied. The enlargement of early endosomes induced by C910 treatment shows phenomenological similarity with the overactivation of Rab5 small GTPase signaling (Stenmark et al., 1994) or the inhibition of the phosphoinositide 5-kinase PIKfyve that synthesizes phosphatidylinositol 3,5-bisphosphate PtdIns $(3,5)P_2$ from PtdIns(3)P on early endosomes (Jefferies et al., 2008). Notably, knockdown of PIKfyve also affects retrograde trafficking from early endosomes to the TGN, and PIKfyve inhibitors protect cells against SARS-CoV-2 (Ou et al., 2020; Riva et al., 2020; Rutherford et al., 2006). Nevertheless, PIKfyve inhibition by apilimod did not protect cells against CNF1 but it did trigger early endosome enlargement in the nanomolar range. Moreover, we found that C910 has no inhibitory effect on recombinant PIKfyve kinase activity *in vitro*. Together, these data indicate that C910 and apilimod diverge in terms of their molecular mechanism of action although both molecules affect the size of EEA1-positive early endosomes and display anti-infective properties. Future characterization of the cellular target of C910 will thus contribute to defining key steps in the vesicular trafficking exploited by numerous bacterial toxins and viruses.

We previously screened 1,120 off-patent drugs from the Prestwick Chemical Library for their ability to protect cells against CNF1-induced Rac1 depletion for drug repurposing (Mahtal et al., 2018, 2020). Nevertheless, the identified compounds did not allow further development in the clinic. Indeed, their antitoxin activities required concentrations above their safety range, and in some instances, they had effects on multiple cellular organelles (Mahtal et al., 2018, 2020). The extended spectrum of protection conferred by C910 here points to its valuable pharmacological properties as much as it displays protection against IAV H1N1 without detectable toxicity in animals. As found for UPEC, C910 might protect cells from infection by bacterial pathogens that are responsible for severe or highly prevalent infections with limited susceptibility to antibiotics. The development of host-directed therapy is also of interest for infections caused by Stx-producing *E. coli* (STEC), as the hemolytic and uremic syndrome caused by the release of the toxin cannot be treated by antibiotics (Tarr et al., 2005), or CNF1-producing UPEC, for which antimicrobial resistance is a growing concern (Mühlen and Dersch, 2016). Interestingly, we showed that C910 displays a higher protection against Stx2 than Stx1. Each toxin hijacks different early endosome-Golgi transport pathways, although Stx2, rather than Stx1, is more likely a critical determinant responsible for hemolytic and uremic syndrome following infection by STEC (Selyunin et al., 2017). Owing to the synthesis of LCGTs, *C. difficile* induces antibiotic and healthcare-associated diarrhea with an approximately 10% mortality rate and a high recurrence rate of approximately 20%. Thus, there is an urgent need to identify novel treatments targeting LCGTs (Johnson and Gerding, 2018).

Previous studies have shown that a host-directed prophylactic strategy endows antitoxin inhibitors with expanded efficacy against viruses (Dai et al., 2018; Gillespie et al., 2013; Wu et al., 2017; Shtanko et al., 2018). During manuscript revision, the toxin inhibitor ABMA was shown to protect cells and mice against

IAV H1N1 (Liu et al., 2022). In pilot experiments, we found also that C910 protected male mice against IAV, but not female mice (data not shown). This bias likely relates to the reported exacerbation of IAV-associated pathogenesis in female mice (Morgan and Klein, 2019). Moreover, differences in C910 efficacy between male and female mice may reflect differences in PK. The rapid evolution of the influenza virus complicates effective vaccine design; therefore, small molecule inhibitors for the treatment of viral infections are urgently needed. There are a number of antivirals in the clinic or under development, many of which target viral proteins. However, resistance to these antivirals rapidly emerges owing to mutations in the viral proteins (Korber et al., 2020; Riva et al., 2020; Wang et al., 2021). Thus, new host-directed antitoxin and antiviral molecules such as C910 deserve further study.

Interestingly, the biodistribution measurements found that C910 accumulates in the lungs despite low plasmatic concentrations. Irrespective of the subcellular distribution of the molecule in either membranes, cytosol or extracellular matrix, the overall concentrations in the lungs found at 1 and 4 h post-administration are above the *in vitro* EC_{50} and should explain *in vivo* efficacy of the treatment against IAV.

LIMITATIONS OF THE STUDY

Here we report the discovery of a molecule, C910, that protects cells against a broad spectrum of bacterial AB toxins and two respiratory viruses SARS-CoV-2 and Influenza A virus H1N1. This molecule accumulates in mouse lung tissues and protects mice against pulmonary infection by IAV at a dose that did not induce detectable behavioral or metabolic toxicities. As such, by acting at the crossroad of the endolysosomal and retrograde transport pathways, C910 displays an original activity and adds to the toolbox of trafficking inhibitors having distinct spectra of antitoxin and anti-pathogen activities. Further work is underway to assess the *in vivo* impact of C910 on toxin-producing bacteria. At this stage, however, there are two main limitations to pushing the development of C910 toward a drug candidate. First, additional work is needed to identify the cellular target(s) of C910 to fully decipher its mechanism of action. Secondly, C910 would need to be optimized by medicinal chemistry to obtain analogues with improved activities in the submicromolar or preferably in the nanomolar range, together with reduced cytotoxicity in order to obtain the best possible selectivity indexes. Nevertheless, it is classical to find hit molecules from a high throughput screening with activities in the micromolar or even tenth of the micromolar range.

STAR★METHODS

Detailed methods are provided in the online version of this paper and include the following:

- KEY RESOURCES TABLE
- RESOURCE AVAILABILITY
  - Lead contact
  - Materials availability
  - Data and code availability
- EXPERIMENTAL MODEL AND SUBJECT DETAILS
  - Animals
  - Cell culture and bacterial toxins
- METHODS DETAILS
  - Orthogonal screening pipeline
  - Evaluating the efficacy of C910 against intoxication
  - Determination of C910 EC_{50} values for DT, Stx1, Stx2 and PE
  - Determination of C910 CC_{50} values in HUVECs and HeLa cells
  - Western blot analysis
  - CNF1 cell binding analyzed by FACS
  - Fluid-phase endocytosed DQ-BSA transport to lysosomes
  - Immunocytochemistry, confocal imaging and image quantification
  - Electron microscopy
  - Lysotracker accumulation in the acidic compartments
  - *In vitro* PIKfyve activity
  - Bacterial infection experiments
  - IAV infection

- SARS-CoV-2 infection
- C910 dosage and quantification by LC–MS/MS for PK and biodistribution studies
- *In vivo* PK, biodistribution and plasma analysis
- *In vivo* IAV infection

- QUANTIFICATION AND STATISTICAL ANALYSIS

SUPPLEMENTAL INFORMATION

Supplemental information can be found online at https://doi.org/10.1016/j.isci.2022.104537.

ACKNOWLEDGMENTS

We thank Cezarela Hoxha, Laurent Audry, Yuen-Yan Chang, Sylvain Meunier (Institut Pasteur, Paris, France), and Imène Belhaouane (Institut Pasteur, Lille) for technical involvement as well as Caroline Stefani (Benaroya Research Institute, USA), Daniel Ladant (Institut Pasteur, Paris) and Jean-Nicolas Tournier (IRBA) for fruitful discussions. This work was funded by the joint ministerial program of Research and Development against Chemical, Biological, Radiological, Nuclear and Explosive risks (CBRNE), grants from the Agence Nationale de la Recherche (ANR-19-ASTR-0001), Labex IBEID (ANR-10-LABX-62-IBEID), and the French Alternative Energies and Atomic Energy Commission (CEA). N.M., E.P., L.C., and F.V. were supported by DGA-MRIS/AID scholarships with CEA or Pasteur. SIMoS and SCBM are members of the Laboratory of Excellence LERMIT and were supported by a grant from the Agence Nationale de la Recherche (ANR-10-LABX-33).

AUTHOR CONTRIBUTIONS

E.L. and D.G. coordinated the research. J.B. directed the HTS. N.M., J.-C.C. and J.B. operated the HTS and analyzed the results. Y.W. and E.P. performed the cell biology experiments. L.S., Y.W., N.M., E.P., and V.K. performed the C910 efficacy measurements against the toxins. IAV H1N1 experiments were performed by C.D. and S.V. (*in vitro*) and S.S. and M.A. (*in vivo*). SARS-CoV-2 experiments were performed by F.G.-B. and O.S. S.P. and A.M. conceived and performed the bacterial invasion experiments. M.S. and Y.W. performed the electron microscopy experiments. L.C., P.C., R.T., P.B., M.K., P.Br., A.Ma., V.S. and F.T. contributed to the PK, toxicology, and biodistribution studies. G.C. and B.P. performed the *in vitro* PIKfyve activity measurements. M.-R.P. and L.J. supplied LCGTs and STxB, respectively. J.-C.C. and F.V. supplied the chemical compounds. Y.W., D.G. and E.L. drafted the manuscript. All authors read and approved the manuscript.

DECLARATION OF INTERESTS

None of the authors have any financial or other interests related to the submitted work.

Received: November 4, 2021
Revised: April 20, 2022
Accepted: June 1, 2022
Published: July 15, 2022

SUPPORTING CITATIONS

The following reference appears in the Supplemental Information: Azarnia Tehran et al., 2015, Boesze-Battaglia et al., 2020, Buchrieser et al., 2020, Canton and Kima, 2012, Harrison et al., 2016, Kali et al., 2021, Schnell et al., 2016, Secher et al., 2015, Wu et al., 2019, Wu et al., 2020, Zilbermintz et al., 2015.

REFERENCES

Aktories, K., Schwan, C., and Jank, T. (2017). Clostridium difficile toxin biology. Annu. Rev. Microbiol. *71*, 281–307.

Alami, M., Taupiac, M.P., Reggio, H., Bienvenüe, A., and Beaumelle, B. (1998). Involvement of ATP-dependent Pseudomonas exotoxin translocation from a late recycling compartment in lymphocyte intoxication procedure. Mol. Biol. Cell *9*, 387–402.

Azarnia Tehran, D., Zanetti, G., Leka, O., Lista, F., Fillo, S., Binz, T., Shone, C.C., Rossetto, O., Montecucco, C., Paradisi, C., et al. (2015). A novel inhibitor prevents the peripheral neuroparalysis of botulinum neurotoxins. Sci. Rep. *5*, 17513. https://doi.org/10.1038/srep17513.

Baell, J.B., and Holloway, G.A. (2010). New substructure filters for removal of pan assay interference compounds (PAINS) from screening libraries and for their exclusion in bioassays. J. Med. Chem. *53*, 2719–2740.

Bassik, M.C., Kampmann, M., Lebbink, R.J., Wang, S., Hein, M.Y., Poser, I., Weibezahn, J., Horlbeck, M.A., Chen, S., Mann, M., et al. (2013). A systematic mammalian genetic interaction map reveals pathways underlying ricin susceptibility. Cell *152*, 909–922.

Biquand, E., Poirson, J., Karim, M., Declercq, M., Malausse, N., Cassonnet, P., Barbezange, C., Straub, M.L., Jones, L., Munier, S., et al. (2017). Comparative profiling of ubiquitin proteasome system interplay with influenza A virus PB2

polymerase protein recapitulating virus evolution in humans. mSphere *2*. e00330–17.

Boesze-Battaglia, K., Dhingra, A., Walker, L.M., Zekavat, A., and Shenker, B.J. (2020). Internalization and intoxication of human macrophages by the active subunit of the aggregatibacter actinomycetemcomitans cytolethal distending toxin is dependent upon cellugyrin (Synaptogyrin-2). Front. Immunol. *11*, 1262.

Bradley, K.A., Mogridge, J., Mourez, M., Collier, R.J., and Young, J.A. (2001). Identification of the cellular receptor for anthrax toxin. Nature *414*, 225–229.

Buchrieser, J., Dufloo, J., Hubert, M., Monel, B., Planas, D., Rajah, M.M., Planchais, C., Porrot, F., Guivel-Benhassine, F., Van der Werf, S., et al. (2020). Syncytia formation by SARS-CoV-2-infected cells. EMBO J. *39*, e106267. https://doi.org/10.15252/embj.2020106267.

Burns, M.C., Howes, J.E., Sun, Q., Little, A.J., Camper, D.V., Abbott, J.R., Phan, J., Lee, T., Waterson, A.G., Rossanese, O.W., and Fesik, S.W. (2018). High-throughput screening identifies small molecules that bind to the RAS:SOS:RAS complex and perturb RAS signaling. Anal. Biochem. *548*, 44–52.

Canton, J., and Kima, P.E. (2012). Targeting host syntaxin-5 preferentially blocks Leishmania parasitophorous vacuole development in infected cells and limits experimental Leishmania infections. Am. J. Pathol. *181*, 1348–1355. https://doi.org/10.1016/j.ajpath.2012.06.041.

Caprioli, A., Donelli, G., Falbo, V., Possenti, R., Roda, L.G., Roscetti, G., and Ruggeri, F.M. (1984). A cell division-active protein from E. coli. Biochem. Biophys. Res. Commun. *118*, 587–593.

Chen, P., Zeng, J., Liu, Z., Thaker, H., Wang, S., Tian, S., Zhang, J., Tao, L., Gutierrez, C.B., Xing, L., et al. (2021). Structural basis for CSPG4 as a receptor for TcdB and a therapeutic target in Clostridioides difficile infection. Nat. Commun. *12*, 3748.

Chicanne, G., Severin, S., Boscheron, C., Terrisse, A.D., Gratacap, M.P., Gaits-Iacovoni, F., Tronchère, H., and Payrastre, B. (2012). A novel mass assay to quantify the bioactive lipid PtdIns3P in various biological samples. Biochem. J. *447*, 17–23.

Collier, R.J., and Young, J.A. (2003). Anthrax toxin. Annu. Rev. Cell Dev. Biol. *19*, 45–70. https://doi.org/10.1146/annurev.cellbio.19.111301.140655.

Contamin, S., Galmiche, A., Doye, A., Flatau, G., Benmerah, A., and Boquet, P. (2000). The p21 Rho-activating toxin cytotoxic necrotizing factor 1 is endocytosed by a clathrin-independent mechanism and enters the cytosol by an acidic-dependent membrane translocation step. Mol. Biol. Cell *11*, 1775–1787.

Dai, W., Wu, Y., Bi, J., Wang, S., Li, F., Kong, W., Barbier, J., Cintrat, J.C., Gao, F., Gillet, D., et al. (2018). Antiviral effects of ABMA against herpes simplex virus type 2 in vitro and in vivo. Viruses *10*, 119.

Diabate, M., Munro, P., Garcia, E., Jacquel, A., Michel, G., Obba, S., Goncalves, D., Luci, C., Marchetti, S., Demon, D., et al. (2015). Escherichia coli alpha-hemolysin counteracts the anti-virulence innate immune response triggered by the Rho GTPase activating toxin CNF1 during bacteremia. PLoS Pathog. *11*, e1004732. https://doi.org/10.1371/journal.ppat.1004732.

Dou, D., Revol, R., Östbye, H., Wang, H., and Daniels, R. (2018). Influenza A virus cell entry, replication, virion assembly and movement. Front. Immunol. *9*, 1581.

Doye, A., Mettouchi, A., Bossis, G., Clement, R., Buisson-Touati, C., Flatau, G., Gagnoux, L., Piechaczyk, M., Boquet, P., and Lemichez, E. (2002). CNF1 exploits the ubiquitin-proteasome machinery to restrict Rho GTPase activation for bacterial host cell invasion. Cell *111*, 553–564.

Ernst, K., Schmid, J., Beck, M., Hägele, M., Hohwieler, M., Hauff, P., Uckert, A.K., Anastasia, A., Fauler, M., Jank, T., et al. (2017). Hsp70 facilitates trans-membrane transport of bacterial ADP-ribosylating toxins into the cytosol of mammalian cells. Sci. Rep. *7*, 2724.

Falzano, L., Fiorentini, C., Donelli, G., Michel, E., Kocks, C., Cossart, P., Cabanie, L., Oswald, E., and Boquet, P. (1993). Induction of phagocytic behaviour in human epithelial cells by Escherichia coli cytotoxic necrotizing factor type 1. Mol. Microbiol. *9*, 1247–1254.

Flatau, G., Lemichez, E., Gauthier, M., Chardin, P., Paris, S., Fiorentini, C., and Boquet, P. (1997). Toxin-induced activation of the G protein p21 Rho by deamidation of glutamine. Nature *387*, 729–733.

Forrester, A., Rathjen, S.J., Daniela Garcia-Castillo, M., Bachert, C., Couhert, A., Tepshi, L., Pichard, S., Martinez, J., Munier, M., Sierocki, R., et al. (2020). Functional dissection of the retrograde Shiga toxin trafficking inhibitor Retro-2. Nat. Chem. Biol. *16*, 327–336.

Gillespie, E.J., Ho, C.L., Balaji, K., Clemens, D.L., Deng, G., Wang, Y.E., Elsaesser, H.J., Tamilselvam, B., Gargi, A., Dixon, S.D., et al. (2013). Selective inhibitor of endosomal trafficking pathways exploited by multiple toxins and viruses. Proc. Natl. Acad. Sci. USA *110*, E4904–E4912.

Gordon, D.E., Jang, G.M., Bouhaddou, M., Xu, J., Obernier, K., O'Meara, M.J., Guo, J.Z., Swaney, D.L., Tummino, T.A., Hüttenhain, R., et al. (2020). A SARS-CoV-2-human protein-protein interaction map reveals drug targets and potential drug-repurposing. Nature *583*, 459–468.

Gupta, N., Noël, R., Goudet, A., Hinsinger, K., Michau, A., Pons, V., Abdelkafi, H., Secher, T., Shima, A., Shtanko, O., et al. (2017). Inhibitors of retrograde trafficking active against ricin and Shiga toxins also protect cells from several viruses, Leishmania and Chlamydiales. Chem. Biol. Interact. *267*, 96–103.

Halabi-Cabezon, I., Huelsenbeck, J., May, M., Ladwein, M., Rottner, K., Just, I., and Genth, H. (2008). Prevention of the cytopathic effect induced by Clostridium difficile Toxin B by active Rac1. FEBS Lett. *582*, 3751–3756.

Hardt, W.D., Chen, L.M., Schuebel, K.E., Bustelo, X.R., and Galan, J.E. (1998). S. typhimurium encodes an activator of Rho GTPases that induces membrane ruffling and nuclear responses in host cells. Cell *93*, 815–826.

Harrison, K., Haga, I.R., Pechenick Jowers, T., Jasim, S., Cintrat, J.-C., Gillet, D., Schmitt-John, T., Digard, P., and Beard, P.M. (2016). Vaccinia virus uses retromer-independent cellular retrograde transport pathways to facilitate the wrapping of intracellular mature virions during virus morphogenesis. J. Virol. *90*, 10120–10132.

Haywood, E.E., Handy, N.B., Lopez, J.W., Ho, M., and Wilson, B.A. (2021). Insertion-trigger residues differentially modulate endosomal escape by cytotoxic necrotizing factor toxins. J. Biol. Chem. *297*, 101347.

Ho, M., Mettouchi, A., Wilson, B.A., and Lemichez, E. (2018). CNF1-like deamidase domains: common Lego bricks among cancer-promoting immunomodulatory bacterial virulence factors. Pathog. Dis. *76*. https://doi.org/10.1093/femspd/fty045.

Jefferies, H.B., Cooke, F.T., Jat, P., Boucheron, C., Koizumi, T., Hayakawa, M., Kaizawa, H., Ohishi, T., Workman, P., Waterfield, M.D., and Parker, P.J. (2008). A selective PIKfyve inhibitor blocks PtdIns(3,5)P(2) production and disrupts endomembrane transport and retroviral budding. EMBO Rep. *9*, 164–170.

Johannes, L., and Romer, W. (2010). Shiga toxins–from cell biology to biomedical applications. Nat. Rev. Microbiol. *8*, 105–116.

Johnson, S., and Gerding, D.N. (2018). Bezlotoxumab. Clin. Infect. Dis. *68*, 699–704.

Kali, S., Jallet, C., Azebi, S., Cokelaer, T., Da Fonseca, J.P., Wu, Y., Barbier, J., Cintrat, J.-C., Gillet, D., and Tordo, N. (2021). Broad spectrum compounds targeting early stages of rabies virus (RABV) infection. Antivir. Res. *188*, 105016.

Kaufmann, S.H.E., Dorhoi, A., Hotchkiss, R.S., and Bartenschlager, R. (2018). Host-directed therapies for bacterial and viral infections. Nat. Rev. Drug Discov. *17*, 35–56.

Klein, R.D., and Hultgren, S.J. (2020). Urinary tract infections: microbial pathogenesis, host-pathogen interactions and new treatment strategies. Nat. Rev. Microbiol. *18*, 211–226.

Korber, B., Fischer, W.M., Gnanakaran, S., Yoon, H., Theiler, J., Abfalterer, W., Hengartner, N., Giorgi, E.E., Bhattacharya, T., Foley, B., et al. (2020). Tracking changes in SARS-CoV-2 spike: evidence that D614G increases infectivity of the COVID-19 virus. Cell *182*, 812–827.e19. https://doi.org/10.1016/j.cell.2020.06.043.

Kounnas, M.Z., Morris, R.E., Thompson, M.R., FitzGerald, D.J., Strickland, D.K., and Saelinger, C.B. (1992). The alpha 2-macroglobulin receptor/low density lipoprotein receptor-related protein binds and internalizes Pseudomonas exotoxin A. J. Biol. Chem. *267*, 12420–12423.

Liu, H., Jiang, C., Wu, Y., Wu, M., Wu, J., Zhao, G., Sun, J., Huang, X., Li, J., Sheng, R., et al. (2022). Antiviral effects of ABMA and DABMA against influenza virus in vitro and in vivo via regulating

the endolysosomal pathway and autophagy. Int. J. Mol. Sci. *23*, 3940.

Mahtal, N., Brewee, C., Pichard, S., Visvikis, O., Cintrat, J.C., Barbier, J., Lemichez, E., and Gillet, D. (2018). Screening of drug library identifies inhibitors of cell intoxication by CNF1. ChemMedChem *13*, 754–761.

Mahtal, N., Wu, Y., Cintrat, J.-C., Barbier, J., Lemichez, E., and Gillet, D. (2020). Revisiting old Ionophore Lasalocid as a novel inhibitor of multiple toxins. Toxins *12*, 26.

Mallard, F., and Johannes, L. (2003). Shiga toxin B-subunit as a tool to study retrograde transport. Methods Mol. Med. *73*, 209–220.

Mallard, F., Tang, B.L., Galli, T., Tenza, D., Saint-Pol, A., Yue, X., Antony, C., Hong, W., Goud, B., and Johannes, L. (2002). Early/recycling endosomes-to-TGN transport involves two SNARE complexes and a Rab6 isoform. J. Cell Biol. *156*, 653–664.

Matrosovich, M., Matrosovich, T., Garten, W., and Klenk, H.D. (2006). New low-viscosity overlay medium for viral plaque assays. Virol. J. *3*, 63.

Michalska, M., and Wolf, P. (2015). Pseudomonas Exotoxin A: optimized by evolution for effective killing. Front. Microbiol. *6*, 963.

Mitra, P. (2020). Inhibiting fusion with cellular membrane system: therapeutic options to prevent severe acute respiratory syndrome coronavirus-2 infection. Am. J. Physiol. Cell Physiol. *319*, C500–C509.

Moreau, D., Kumar, P., Wang, S.C., Chaumet, A., Chew, S.Y., Chevalley, H., and Bard, F. (2011). Genome-wide RNAi screens identify genes required for Ricin and PE intoxications. Dev. Cell *21*, 231–244.

Morgan, R., and Klein, S.L. (2019). The intersection of sex and gender in the treatment of influenza. Curr. Opin. Virol. *35*, 35–41.

Mühlen, S., and Dersch, P. (2016). Anti-virulence strategies to target bacterial infections. Curr. Top. Microbiol. Immunol. *398*, 147–183.

Nelson, E.A., Dyall, J., Hoenen, T., Barnes, A.B., Zhou, H., Liang, J.Y., Michelotti, J., Dewey, W.H., DeWald, L.E., Bennett, R.S., et al. (2017). The phosphatidylinositol-3-phosphate 5-kinase inhibitor apilimod blocks filoviral entry and infection. PLoS Negl Trop Dis *11*, e0005540.

Ou, X., Liu, Y., Lei, X., Li, P., Mi, D., Ren, L., Guo, L., Guo, R., Chen, T., Hu, J., et al. (2020). Characterization of spike glycoprotein of SARS-CoV-2 on virus entry and its immune cross-reactivity with SARS-CoV. Nat. Commun. *11*, 1620. https://doi.org/10.1038/s41467-020-15562-9.

Papatheodorou, P., Barth, H., Minton, N., and Aktories, K. (2018). Cellular uptake and mode-of-action of Clostridium difficile toxins. Adv. Exp. Med. Biol. *1050*, 77–96.

Papini, E., Rappuoli, R., Murgia, M., and Montecucco, C. (1993). Cell penetration of diphtheria toxin. Reduction of the interchain disulfide bridge is the rate-limiting step of translocation in the cytosol. J. Biol. Chem. *268*, 1567–1574.

Petty, N.K., Ben Zakour, N.L., Stanton-Cook, M., Skippington, E., Totsika, M., Forde, B.M., Phan, M.D., Gomes Moriel, D., Peters, K.M., Davies, M., et al. (2014). Global dissemination of a multidrug resistant Escherichia coli clone. Proc. Natl. Acad. Sci. USA *111*, 5694–5699.

Pierzyńska-Mach, A., Janowski, P.A., and Dobrucki, J.W. (2014). Evaluation of acridine orange, LysoTracker Red, and quinacrine as fluorescent probes for long-term tracking of acidic vesicles. Cytometry *85*, 729–737.

Piteau, M., Papatheodorou, P., Schwan, C., Schlosser, A., Aktories, K., and Schmidt, G. (2014). Lu/BCAM adhesion glycoprotein is a receptor for Escherichia coli cytotoxic necrotizing factor 1 (CNF1). PLoS Pathog. *10*, e1003884.

Ratts, R., Zeng, H., Berg, E.A., Blue, C., McComb, M.E., Costello, C.E., vanderSpek, J.C., and Murphy, J.R. (2003). The cytosolic entry of diphtheria toxin catalytic domain requires a host cell cytosolic translocation factor complex. J. Cell Biol. *160*, 1139–1150.

Riva, L., Yuan, S., Yin, X., Martin-Sancho, L., Matsunaga, N., Pache, L., Burgstaller-Muehlbacher, S., De Jesus, P.D., Teriete, P., Hull, M.V., et al. (2020). Discovery of SARS-CoV-2 antiviral drugs through large-scale compound repurposing. Nature *586*, 113–119.

Rolando, M., Stefani, C., Flatau, G., Auberger, P., Mettouchi, A., Mhlanga, M., Rapp, U., Galmiche, A., and Lemichez, E. (2010). Transcriptome dysregulation by anthrax lethal toxin plays a key role in induction of human endothelial cell cytotoxicity. Cell Microbiol. *12*, 891–905.

Rutherford, A.C., Traer, C., Wassmer, T., Pattni, K., Bujny, M.V., Carlton, J.G., Stenmark, H., and Cullen, P.J. (2006). The mammalian phosphatidylinositol 3-phosphate 5-kinase (PIKfyve) regulates endosome-to-TGN retrograde transport. J. Cell Sci. *119*, 3944–3957.

Sandvig, K., Garred, O., Prydz, K., Kozlov, J.V., Hansen, S.H., and van Deurs, B. (1992). Retrograde transport of endocytosed Shiga toxin to the endoplasmic reticulum. Nature *358*, 510–512.

Sandvig, K., Prydz, K., Hansen, S.H., and van Deurs, B. (1991). Ricin transport in brefeldin A-treated cells: correlation between Golgi structure and toxic effect. J. Cell Biol. *115*, 971–981.

Schmidt, G., Sehr, P., Wilm, M., Selzer, J., Mann, M., and Aktories, K. (1997). Gln 63 of Rho is deamidated by Escherichia coli cytotoxic necrotizing factor-1. Nature *387*, 725–729.

Schnell, L., Mittler, A.-K., Mattarei, A., Tehran, D.A., Montecucco, C., and Barth, H. (2016). Semicarbazone EGA inhibits uptake of diphtheria toxin into human cells and protects cells from intoxication. Toxins *8*, 221. https://doi.org/10.3390/toxins8070221.

Scobie, H.M., Rainey, G.J., Bradley, K.A., and Young, J.A. (2003). Human capillary morphogenesis protein 2 functions as an anthrax toxin receptor. Proc. Natl. Acad. Sci. USA *100*, 5170–5174.

Scott, C.C., Vacca, F., and Gruenberg, J. (2014). Endosome maturation, transport and functions. Semin. Cell Dev. Biol. *31*, 2–10.

Secher, T., Shima, A., Hinsinger, K., Cintrat, J.C., Johannes, L., Barbier, J., Gillet, D., and Oswald, E. (2015). Retrograde trafficking inhibitor of shiga toxins reduces morbidity and mortality of mice infected with enterohemorrhagic Escherichia coli. Antimicrob. Agents Chemother. *59*, 5010–5013. https://doi.org/10.1128/AAC.00455-15.

Selyunin, A.S., Hutchens, S., McHardy, S.F., and Mukhopadhyay, S. (2019). Tamoxifen blocks retrograde trafficking of Shiga toxin 1 and 2 and protects against lethal toxicosis. Life Sci Alliance *2*, e201900439.

Selyunin, A.S., Iles, L.R., Bartholomeusz, G., and Mukhopadhyay, S. (2017). Genome-wide siRNA screen identifies UNC50 as a regulator of Shiga toxin 2 trafficking. J. Cell Biol. *216*, 3249–3262.

Selyunin, A.S., Nieves-Merced, K., Li, D., McHardy, S.F., and Mukhopadhyay, S. (2021). Tamoxifen derivatives alter retromer-dependent endosomal tubulation and sorting to block retrograde trafficking of shiga toxins. Toxins *13*, 424.

Shtanko, O., Sakurai, Y., Reyes, A.N., Noël, R., Cintrat, J.C., Gillet, D., Barbier, J., and Davey, R.A. (2018). Retro-2 and its dihydroquinazolinone derivatives inhibit filovirus infection. Antivir. Res. *149*, 154–163.

Sieczkarski, S.B., and Whittaker, G.R. (2003). Differential requirements of Rab5 and Rab7 for endocytosis of influenza and other enveloped viruses. Traffic *4*, 333–343.

Stechmann, B., Bai, S.K., Gobbo, E., Lopez, R., Merer, G., Pinchard, S., Panigai, L., Tenza, D., Raposo, G., Beaumelle, B., et al. (2010). Inhibition of retrograde transport protects mice from lethal ricin challenge. Cell *141*, 231–242.

Stenmark, H., Parton, R.G., Steele-Mortimer, O., Lütcke, A., Gruenberg, J., and Zerial, M. (1994). Inhibition of rab5 GTPase activity stimulates membrane fusion in endocytosis. EMBO J. *13*, 1287–1296.

Tao, L., Tian, S., Zhang, J., Liu, Z., Robinson-McCarthy, L., Miyashita, S.I., Breault, D.T., Gerhard, R., Oottamasathien, S., Whelan, S.P.J., and Dong, M. (2019). Sulfated glycosaminoglycans and low-density lipoprotein receptor contribute to Clostridium difficile toxin A entry into cells. Nat. Microbiol. *4*, 1760–1769.

Tarr, P.I., Gordon, C.A., and Chandler, W.L. (2005). Shiga-toxin-producing Escherichia coli and haemolytic uraemic syndrome. Lancet *365*, 1073–1086.

Torrino, S., Visvikis, O., Doye, A., Boyer, L., Stefani, C., Munro, P., Bertoglio, J., Gacon, G., Mettouchi, A., and Lemichez, E. (2011). The E3 ubiquitin-ligase HACE1 catalyzes the ubiquitylation of active Rac1. Dev. Cell *21*, 959–965.

Visvikis, O., Boyer, L., Torrino, S., Doye, A., Lemonnier, M., Lores, P., Rolando, M., Flatau, G.,

Mettouchi, A., Bouvard, D., et al. (2011). Escherichia coli producing CNF1 toxin hijacks tollip to trigger rac1-dependent cell invasion. Traffic *12*, 579–590.

von Eichel-Streiber, C., Harperath, U., Bosse, D., and Hadding, U. (1987). Purification of two high molecular weight toxins of Clostridium difficile which are antigenically related. Microb. Pathog. *2*, 307–318.

Wandinger-Ness, A., and Zerial, M. (2014). Rab proteins and the compartmentalization of the endosomal system. Cold Spring Harbor. Perspect. Biol. *6*, a022616.

Wang, P., Liu, L., Iketani, S., Luo, Y., Guo, Y., Wang, M., Yu, J., Zhang, B., Kwong, P.D., Graham, B.S., et al. (2021). Increased Resistance of SARS-CoV-2 Variants B.1.351 and B.1.1.7 to Antibody Neutralization. Preprint at bioRxiv. 2021.02.12.430472. https://doi.org/10.1101/2021.01.25.428137.

Wei, W., Lu, Q., Chaudry, G.J., Leppla, S.H., and Cohen, S.N. (2006). The LDL receptor-related protein LRP6 mediates internalization and lethality of anthrax toxin. Cell *124*, 1141–1154.

Wu, Y., Pons, V., Goudet, A., Panigai, L., Fischer, A., Herweg, J.A., Kali, S., Davey, R.A., Laporte, J., Bouclier, C., et al. (2017). ABMA, a small molecule that inhibits intracellular toxins and pathogens by interfering with late endosomal compartments. Sci. Rep. *7*, 15567.

Wu, Y., Pons, V., Noël, R., Kali, S., Shtanko, O., Davey, R.A., Popoff, M.R., Tordo, N., Gillet, D., Cintrat, J.-C., and Barbier, J. (2019). DABMA: a derivative of ABMA with improved broad-spectrum inhibitory activity of toxins and viruses. ACS Med. Chem. Lett. *10*, 1140–1147. https://doi.org/10.1021/acsmedchemlett.9b00155.

Wu, Y., Boulogne, C., Carle, S., Podinovskaia, M., Barth, H., Spang, A., Cintrat, J.-C., Gillet, D., and Barbier, J. (2020). Regulation of endo-lysosomal pathway and autophagic flux by broad-spectrum antipathogen inhibitor ABMA. FEBS J. *287*, 3184–3199. https://doi.org/10.1111/febs.15201.

Zhou, P., Yang, X.L., Wang, X.G., Hu, B., Zhang, L., Zhang, W., Si, H.R., Zhu, Y., Li, B., Huang, C.L., et al. (2020). A pneumonia outbreak associated with a new coronavirus of probable bat origin. Nature *579*, 270–273.

Zilbermintz, L., Leonardi, W., Jeong, S.-Y., Sjodt, M., McComb, R., Ho, C.-L.C., Retterer, C., Gharaibeh, D., Zamani, R., Soloveva, V., et al. (2015). Identification of agents effective against multiple toxins and viruses by host-oriented cell targeting. Sci. Rep. *5*. https://doi.org/10.1038/srep13476.

STAR★METHODS

KEY RESOURCES TABLE

REAGENT or RESOURCE	SOURCE	IDENTIFIER
Antibodies		
mouse anti-Actin	Sigma	Cat# A2228; RRID:AB_476697
rabbit anti-EEA1	Cell signaling	Cat#3288; RRID:AB_2096811
rabbit anti-Rab7	Cell signaling	Cat#9367; RRID:AB_1904103
rabbit-anti-his tag	Cell signaling	Cat#12698; RRID:AB_2744546
rabbit anti-Rab7	Abcam	Cat#ab137029; RRID:AB_2629474
mouse anti-Giantin	Abcam	Cat#ab37266; RRID:AB_880195
mouse-anti-6×-his [clone 3D5]	Thermo	Cat# R930-25; RRID:AB_2556553
mouse-anti-EEA1	BD Bioscience	Cat#610457; RRID:AB_397830
mouse-anti-Rab5	BD Bioscience	Cat#610724; RRID:AB_398047
mouse anti-Rac1 [clone 102]	BD Bioscience	Cat#610651; RRID:AB_397978
mouse anti-Rab4	BD Bioscience	Cat#610888; RRID:AB_398205
mouse anti-Lamp1	BD Bioscience	Cat#611043; RRID:AB_398356
mouse anti-TGN38	Santa Cruz	Cat#sc-101273; RRID:AB_1130226
rabbit anti-MEK-2	Santa Cruz	Cat#sc-524; RRID:AB_2281672
mouse anti-Rho A [clone 26C4]	Santa Cruz	Cat#sc-418; RRID:AB_628218
rabbit anti-Calnexin	Enzo	Cat#ADI-SPA-860-D; RRID:AB_2038898
mouse-anti-LBPA	Echelon Biosciences	Cat#Z-PLBPA; RRID:AB_11129226
Alexa Fluor 594 donkey anti-mouse	Thermo Fisher	Cat#A-21203; RRID:AB_141633
Alexa Fluor 594 donkey anti-rabbit	Thermo Fisher	Cat#A-21207; RRID:AB_141637
Alexa Fluor 488 donkey anti-mouse	Thermo Fisher	Cat#A-21202; RRID:AB_141607
Alexa Fluor 488 donkey anti-rabbit	Thermo Fisher	Cat#A-21206; RRID:AB_2535792
Alexa Fluor 647 donkey anti-mouse	Thermo Fisher	Cat#A-31571; RRID:AB_162542
Horseradish peroxidase (HRP)-conjugated goat anti-mouse secondary antibodies	Dako	Cat#P0447; RRID:AB_2617137
Horseradish peroxidase (HRP)-conjugated swine anti-rabbit secondary antibodies	Dako	Cat#P0399; RRID:AB_2617141
Mouse anti-GAPDH	Santa Cruz	Cat#sc-47724; RRID:AB_627678
Bacterial and virus strains		
Uropathogenic *E. coli*	This manuscript	UTI89
Salmonella enterica serovar Typhimurium	This manuscript	SL1344
$H1N1_{pdm09}$	This manuscript	SeasonalA/Bretagne/7608/2009
SARS-CoV-2	This manuscript	BetaCoV/France/IDF0372/2020
Biological samples		
Mouse lung samples	This study	N/A
Mouse blood samples	This study	N/A
Chemicals, peptides, and recombinant proteins		
C910	ChemBridge	ID: 5454910
C910	Synthenova	ID: SN0218L3
L-[^{14}C(U)]-leucine	Perkin-Elmer	Cat#NEC279E050UC
Hoechst 33342	Sigma	Cat#B2261
Gelatin	Sigma	Cat#G9361

(*Continued on next page*)

Continued

REAGENT or RESOURCE	SOURCE	IDENTIFIER
Saponin	Sigma	Cat#S-7900
Bafilomycin A1	Sigma	Cat#B1793
Rasazurin	Sigma	Cat#R7017
Apilimod	Sigma	Cat#A149227
Paraformaldehyde (PFA)	Electron Microscopy Science	Cat#15710
CNF1	This manuscript	See method details
DT	Sigma-Aldrich	Cat#D0564
Stx1	List Biological	Cat#161
Stx2	List Biological	Cat#162
PE toxin	Bruno Beaumelle (UMR5236 CNRS, University of Montpellier, France)	See method details
TcdA and TcdB purified from *C. difficile* VPI10463	This manuscript	See method details
Protective antigen and lethal factor from *B.anthracis*	This manuscript	See method details
STxB labeled with Alexa Fluor 488	This manuscript	See method details
CNF1 labeled with Cy3	This manuscript	See method details
Critical commercial assays		
Cathepsin B activity assay kit	Abcam	Cat#ab65300
DQ™ Red BSA	Thermo Fisher Scientific	Cat#D-112051
LysoTracker® Red DND-99	Thermo Fisher Scientific	Cat#L7528
Cy3® Mono 5-pack	GE Healthcare	Cat#PA23001
BSA-gold	Cell Microscopy Core	Cat#BSAG 5nm
Experimental models: Cell lines		
HUVECs	PromoCell	Cat#C-12203
HeLa with homogenous Gb3 expression	This manuscript	See method details
L929	ATCC	Cat# CCL-1
A549	ATCC	Cat# CCL-185™
Vero E6	Sigma	Cat#685020206
U2OS-ACE2 GFP1-10 and GFP 11 cells	This manuscript	See method details
Experimental models: Organisms/strains		
C57BL/6 male mice	Charles River Laboratories	JAX: 000664
C57BL/6J male mice	Janvier Labs	C57BL/6JRj
Software and algorithms		
GraphPad Prism 6 or 8.3	GraphPad Software	https://www.graphpad.com/scientificsoftware/prism/
Fiji software	NIH	https://imagej.nih.gov/ij/
FlowJo	BD Bioscience	https://www.flowjo.com/

RESOURCE AVAILABILITY

Lead contact

Further requests for resources, reagents and original data should be directed to and will be fulfilled by the lead contact, Emmanuel Lemichez (emmanuel.lemichez@pasteur.fr).

Materials availability

This work did not generate new unique reagents.

Data and code availability

- All data reported in this paper will be shared by the lead contact upon request.
- This paper does not report original codes.
- Any additional information required to re-analyze the data reported in this paper is available from the lead contact upon request.

EXPERIMENTAL MODEL AND SUBJECT DETAILS

Animals

For IAV infection, all mice were housed under specific-pathogen-free conditions at Seattle Children's Research Institute, and all animal experiments performed at Seattle Children's Research Institute were approved by the Institutional Animal Care and Use Committee (IACUC00580). To minimize suffering, mice were monitored daily and euthanized when they showed significant weight loss (greater than 20%) or exhibited signs of immobility or severe difficulty of breathing. A pilot experiment showed a protective effect of C910 in male animals; therefore, we used male mice for further experiments (data not shown).

Cell culture and bacterial toxins

Human umbilical vein endothelial cells (HUVECs) (PromoCell, Heidelberg, Germany) were cultured in human endothelial SFM, supplemented with 20% fetal bovine serum, 20 ng/mL bFGF,10 ng/mL EGF, 1 μg/mL Heparin and 100 U/mL penicillin- 100 μg/mL streptomycin (Torrino et al., 2011). HeLa cell (a clone with homogeneous Gb3 expression), L929, Vero, A549, Vero E6 and U2OS-ACE2 cells were cultured at 37°C with 5% CO_2 in DMEM/GlutaMAX (Invitrogen) supplemented with 10% heat-inactivated FBS (F9665, Sigma–Aldrich) and 1% penicillin/streptomycin (Invitrogen).

DT (D0564) was purchased from Sigma-Aldrich, Stx1 (#161) and Stx2 (#162) were from List Biological. CNF1 was purified as described (Mahtal et al., 2018), TcdA and TcdB were purified from *C. difficile* VPI10463 (von Eichel-Streiber et al., 1987), and protective antigen and lethal factor from *B. anthracis* were purified as described (Rolando et al., 2010). PE toxin was kindly provided by Bruno Beaumelle (UMR5236 CNRS, University of Montpellier, France). STxB was purified and labeled with Alexa Fluor 488 (Mallard et al., 2002; Mallard and Johannes, 2003).

METHODS DETAILS

Orthogonal screening pipeline

All steps of the compound screening were performed in gelatin-coated Nunc Micro-Well 96-well opaque plates (Thermo Scientific) seeded with 20,000 HUVECs per well. During the first round of screening, we tested 16,840 compounds from the ChemBridge DIVERSet library at a working concentration of 50 μM in the presence of 10 nM CNF1 for 6 h (Z′ values >0.5).

$$Z' = 1 - \frac{(3SDx + 3SDy)}{\text{mean } (x) \text{ mean } (y)}$$

Rac1 cellular levels were determined by direct immunolabeling as follows. HUVEC fixation was performed in 4% PFA for 15 min. Permeabilization and saturation were performed concomitantly in D-PBS supplemented with 1% donkey serum, 0.1% Triton X-100 and 0.05% Tween -20 for 1 h. Cells were next labeled with an anti-Rac1 mouse antibody [clone 102] for 1 h and revealed with an Alexa Fluor 488-coupled anti-mouse secondary antibody. Rac1 immunostaining was quantified using a Cytation 5 reader (BioTek) in fluorescence intensity mode (λ_{Ex}= 485 nm; λ_{Em}= 520 nm) with a 3 × 3 area scan mode per well. Hit compounds were chosen and reevaluated following the same procedure with another secondary antibody coupled with Alexa Fluor 594 (λ_{Ex}= 590 nm; λ_{Em}= 620 nm) to exclude autofluorescent molecules. Selected hits were then reordered and freshly prepared for a third round of screening. The hit compounds were further filtered from pan-assay interference compounds (PAINS), i.e., unstable molecules, irreversible modifiers or compounds that are frequently active in other screens (Baell and Holloway, 2010). Ten compounds were shortlisted as robust inhibitors of the CNF1-mediated degradation of Rac1 and underwent a series of two orthogonal screens to define their protective effects against DT and Stx1. Two compounds (ChemBridge IDs: 5344639 and 5363116) were identified as inhibitors of DT but not Stx1. N-(3,3-diphenylpropyl)-1-propyl-4-piperidinamine, herein referred to as C910 ($C_{20}H_{26}N_2$), passed all of the screens against CNF1, DT and Stx1. C910 shows lypophylicity with a partitioning coefficient (octanol/water) log p = 4.53.

Of note, C910 and the unrelated compound (S)-2-amino-N-(1-((5-chloro-1*H*-indol-3-yl)methyl)piperidin-4-yl)-3-(1*H*-indol-3-yl) propanamide (referred to as API or SN0209) have been isolated for their capacity to alter the interaction of SOS with p21-Ras GTPase *in vitro* (Burns et al., 2018). Cotreatment of cells with 5 to 10 μM API did not protect the cells from CNF1, ruling out a possible protective action of C910 through SOS/Ras signaling (not shown).

Evaluating the efficacy of C910 against intoxication

Protein synthesis inhibition was determined by scintillation counting of the amount of L-[^{14}C(U)]-leucine incorporated in cells (Stechmann et al., 2010). Briefly, cells were plated overnight in 96-well Cytostar-T microplates with a scintillator incorporated into the polystyrene. Cells were then challenged with increasing doses of toxins for the indicated periods of time (DT: 6 h; Stx1, Stx2, PE: 18 h) in the presence of vehicle or various concentrations of C910. The medium was replaced with DMEM supplemented with 0.5 μCi/mL L-[^{14}C(U)]-leucine for an additional 3 h (Stx1, Stx2, PE) or 15 h (DT). Protein synthesis was determined using a Wallac 1,450 Micro-Beta scintillation counter (PerkinElmer). All values are expressed as the means of duplicate measurements ± s.d.; data were fitted using the nonlinear regression dose–response, and the goodness-of-fit values for the toxin alone (carrier) or toxin with drug were assessed by r^2 values and confidence intervals with Prism ver. 8 software (GraphPad, San Diego, CA).

The cytotoxic effects of the LCGTs TcdA and TcdB on Vero cells (Sigma-Aldrich) were evaluated by measuring cell rounding with phase-contrast microscopy. Vero cells seeded in 96-well plates at a density of 10,000 cells per well one day prior to the experiment were intoxicated with 8 cytotoxic units of TcdA or TcdB for 8 h in the presence of DMSO vehicle or C910 at 0, 5, 10 and 20 μM. One cytotoxic unit of TcdA (~10 ng) or TcdB (~1 pg) was defined as the amount of active toxin required to induce 100% rounding in 10,000 Vero cells in 18 h. In parallel, cell lysates from intoxicated cells were examined for glucosylated Rac1, which no longer reacts to the anti-Rac1 monoclonal antibody [clone 102].

The activity of LT from *B. anthracis* was assessed by determining MEK2 cleavage. Cell lysates from HUVECs intoxicated with two concentrations of LT (0.3 μg/mL protective antigen (PA) + 0.1 μg/mL lethal factor (LF) or 0.03 μg/mL PA + 0.1 μg/mL LF) in the absence or presence of C910 at 40 μM for 1, 2, 4, and 8 h were collected and examined for MEK2 protein levels by immunoblotting. GAPDH was used as the loading control.

Determination of C910 EC_{50} values for DT, Stx1, Stx2 and PE

The mean percentage of protein biosynthesis was determined and normalized from duplicate wells. All values are expressed as the means ± s.d. Data were fitted with Prism v8 software (GraphPad Inc., San Diego, CA) to obtain the toxin concentrations that inhibited 50% of protein synthesis in the absence or presence of compound ($IC_{50\ drug}$ vs $IC_{50\ DMSO}$). The protection Factors R (R = $IC_{50\ drug}/IC_{50\ DMSO}$) were determined by the software's nonlinear regression "dose-response EC_{50} shift equation". For each concentration of C910, the percent protection was determined from the R values (% protection = (R-1)/(R_{max} − 1) × 100, with R_{max} corresponding to the highest value of R in the series). The concentration of C910 was plotted against the corresponding percent cell protection, and the 50% effective concentration (EC_{50}) was calculated by nonlinear regression (R squared > 0.95).

Determination of C910 CC_{50} values in HUVECs and HeLa cells

10,000 Cells seeded in 96-well flat clear bottom black microplates, were incubated with increasing doses of C910 for 6 h, then the medium was replaced with fresh medium containing Resazurin (1/250). The fluorescence (540 nm /580 nm) was measured with FluoStar Omega (BMG Labtech). 0.5% Triton X-100-treated cells was a positive control for cell death. The percentage of viability was expressed as the mean ± s.d. from four replicate wells of one representative experiment (n = 3). The concentration of C910 was plotted against the corresponding percent cell viability, and the 50% effective concentration (CC_{50}) was calculated by nonlinear regression (R squared > 0.95).

Western blot analysis

Samples were size-separated via SDS-PAGE, transferred to Immobilon-P PVDF membranes (Millipore) and labeled with primary antibodies. Signals were revealed using horseradish peroxidase-conjugated goat anti-mouse or swine anti-rabbit secondary antibodies (DAKO) followed by chemiluminescence using

Immobilon® Western (Millipore). Chemiluminescent signals were recorded with a Syngene PXi imager (OZYME), and the data were quantified using Fiji software (NIH).

CNF1 cell binding analyzed by FACS

Recombinant CNF1 toxin was fluorescently labeled with Cy3 (Cy3® Mono 5-pack, GE Healthcare, PA23001) according to the vendor's recommendations. Briefly, purified toxin preparations (1 mg/mL) were incubated with Cy3 dye in 100 mM bicarbonate buffer for 18 h at 4 °C and subjected to dialysis to separate the toxin from the free dye. CNF1-Cy3 (16 nM) was allowed to bind to the cells at 4 °C for 30 min, and the cells were processed for FACS analysis using a BD LSRFortessa™ flow cytometer. Data were analyzed with FlowJo (BD Bioscience).

Fluid-phase endocytosed DQ-BSA transport to lysosomes

HUVECs were seeded in fibronectin-pretreated μ-Slide 8 Well Glass Bottom (80827, ibidi) one day prior to the experiments. Cells were pulsed with DQ-BSA (DQ™ Red BSA) at a concentration of 10 μg/mL for 30 min (37 °C, 5% CO_2). The cells were then washed three times with PBS before being treated with compounds in complete medium at 37 °C for the indicated time. The fluorescence of the live cells was measured with a Perkin Elmer Ultraview spinning disk confocal microscope using a 60×/1.2 NA water objective.

Immunocytochemistry, confocal imaging and image quantification

Immunocytochemistry was performed on cells fixed with 4% PFA in PBS for 15 min at room temperature. Next, the cells were permeabilized with 0.1% saponin in PBS for 10 min and blocked with 0.2% gelatin in PBS. Immunolabeling with the indicated antibodies was performed in 0.05% saponin and 0.1% gelatin in PBS. Images were acquired with a Perkin Elmer Ultraview spinning disk confocal microscope using a 60×/1.2 NA oil objective. Fiji ImageJ software (NIH) was used for image processing and quantification.

The colocalization of two fluorescence signals of interest were measured, and the results are expressed as a Pearson's coefficient correlation or a Mander's overlap coefficient. Cells from each set of experimental conditions were randomly selected and analyzed with the same threshold. Briefly, individual cells were selected from a single mid-z stack of the confocal image by hand-drawing a region of interest (ROI) with Fiji software. The two fluorescent channels were then separated and analyzed with the JACop plug-in.

The sizes of the EEA1-positive vesicles were measured from the single mid-z stack of confocal images and were next quantified with the Analyze particles tool in Fiji Software. Threshold values were maintained throughout each experimental set.

Electron microscopy

After the uptake of BSA-gold (Cell Microscopy Core, Universitair Medisch Centrum Utrecht, Netherlands), HUVECs were fixed at room temperature for 2 h in 2.5% glutaraldehyde in PHEM buffer, pH 7.2 (60 mM 1,4 piperazine diethylsulfonic acid (PIPES), 25 mM 4-(2-hydroxyethyl)-1-piperazineethanesulfonic acid (HEPES), 10 mM EGTA, 2 mM $MgCl_2$, pH 7.2). After washes with PHEM, the cells were postfixed with 1% osmium and 1.5% potassium ferricyanide (Merck, Darmstadt, Germany) in PHEM before dehydration with a graded series of ethanol and infiltration with epoxy resin. The resin was polymerized at 60 °C for 48 h. Sections with a nominal thickness of 70 nm were obtained with a UC7 ultramicrotome (Leica Microsystems, Vienna, Austria) and collected on formvar/carbon-coated 200 mesh copper grids (Electron Microscopy Sciences, Hatfield, PA, USA). Sections were contrasted with 4% uranyl acetate and Reynold's lead citrate and observed with a Tecnai Spirit (Thermo Fisher, Eindhoven, Netherlands) operated at 120 kV. Images were acquired using a Gatan Ultra Scan™ 4000 digital camera (Gatan, Pleasanton, USA).

Lysotracker accumulation in the acidic compartments

HUVECs were seeded at a density of 10^3 cells/well in 96-well black plates (Greiner, μClear). The next day, the cells were incubated with the compounds for 2 or 4 h before addition of LysoTracker® Red DND-99 (100 nM) for 15 min. The cells were washed three times with D-PBS prior to fixation with 4% PFA, permeabilization with 0.1% saponin for 10 min and treatment with DAPI at 1 μg/mL for 15 min. Plates were imaged with an Opera Phenix HCS microscope with a 40× water objective. The acquisition conditions were identical for all independent experiments. Fluorescence signals were analyzed with Columbus software (Perkin Elmer). Briefly, the LysoTracker® fluorescence signals in the cytoplasm of each cell were quantified after cell

segmentation with a DAPI mask. Incomplete cells at the edge of the fields were excluded from the analysis. We set a threshold of maximum LysoTracker intensity per cell to reach 90% positive cells with DMSO (vehicle) and less than 10% positive cells for the condition BafA1. The percentage of positive cells in each field corresponds to the ratio between the number of cells displaying a signal above the threshold divided by the total number of cells analyzed.

In vitro PIKfyve activity

Recombinant PIKfyve production and activity measurements were performed as described (Chicanne et al., 2012). Briefly, PIKfyve was incubated with DMSO or compound in the presence of PtdIns3P/PE lipid vesicles for 15 min at room temperature prior to the addition of [γ^{32}P]-ATP and incubation at 37 °C for 30 min. After lipid extraction and thin layer chromatography, the amount of [^{32}P]-PtdIns(3,5)P_2 produced by PIKfyve was visualized by autoradiography.

Bacterial infection experiments

Uropathogenic strain UTI89Δ*hlyA*Δ*cnf1* (Diabate et al., 2015) and *Salmonella enterica* serovar Typhimurium strain SL1344, kindly provided by Jost Enninga (Institut Pasteur, France), were used in this assay. Bacterial internalization into HUVECs was assessed using a gentamycin protection assay. Briefly, HUVECs were seeded on 12-well plates at a density of 250,000 cells/well overnight (triplicate wells were set up). When indicated, 1 nM CNF1 toxin was added after 30 min of pretreatment with 15 μM C910. Exponentially growing UPEC (OD_{600} = 0.6 in LB) or *Salmonella* (OD_{600} = 0.6 in LB with 0.3 M NaCl) were added to cells at an MOI of 100, followed by 20 min of centrifugation at 1,000 × g at room temperature. Cell infection was performed for 10 min at 37°C with 5% CO_2. Infected cells were washed three times with PBS and either lysed for cell-bound bacteria measurements or incubated for another 30 min in the presence of 50 μg/mL gentamicin before lysis for internalized bacteria measurements. Cells were lysed in PBS +0.1% Triton X-100, and serially diluted bacteria were plated on LB agar supplemented with 200 μg/mL streptomycin or ML agar for CFU counting.

IAV infection

For single-cycle IAV infection assays, A549 cells (70,000/well) were infected with the reporter H1N1 A/WSN/33 ($H1N1_{WSN}$ PB2-2A-mCitrine) at an MOI of 5 PFU/cell for 6 h. Cells were then fixed in 4% PFA and analyzed by flow cytometry (Attune NxT; Thermo Fisher Scientific) (Biquand et al., 2017). For multicycle growth assays, A549 cells were infected with a seasonal A/Bretagne/7608/2009 ($H1N1_{pdm09}$) strain adapted to human cell lines (Biquand et al., 2017) at an MOI of 10^{-3} infective particles/cell in highly sensitive canine MDCK-SIAT cells, and the production of infectious particles in the culture supernatant was determined at 24 h using a standard plaque assay(Matrosovich et al., 2006).

SARS-CoV-2 infection

U2OS-ACE2 GFP1-10 and GFP 11 cells, also termed S-Fuse cells, become GFP+ after their successful infection with SARS-CoV-2 (Buchrieser et al., 2020)). Cells were mixed (ratio 1:1) and plated at a density of 4×10^3 per well in a μClear 96-well plate (Greiner Bio-One). The following day, the cells were incubated with the indicated concentrations of C910 for 2 h at 37 °C. SARS-CoV-2 (BetaCoV/France/IDF0372/2020) (MOI 0.1) was then added. Twenty hours later, the cells were fixed with 2% PFA, washed and stained with Hoechst 33342 (dilution 1:1,000, Invitrogen). Images were acquired with an Opera Phenix high content confocal microscope (PerkinElmer). The GFP area and the number of nuclei were quantified using Harmony software (PerkinElmer). The percent inhibition was calculated using the GFP area value along with the following formula: 100 × (1 – (value with C910 – value in "non-infected")/(value with " DMSO vehicle" – value in "non-infected")).

C910 dosage and quantification by LC–MS/MS for PK and biodistribution studies

Two stock solutions of the C910 standard and another compound used as an internal MS standard (IS) were prepared at concentrations of 10 mM in DMSO. To establish calibration plots, known amounts of C910 were spiked into control mouse plasma or lung homogenates. To eliminate plasma proteins and other endogenous compounds, C910 was extracted from the plasma samples twice with acetone. This involved the addition of 4 volumes of ice-cold acetone and incubation for 1 h at −20°C. After centrifugation at 15,000 × g for 10 min, the supernatants containing C910 were collected. For each sample, both acetone supernatants were combined and dried at 40°C for 3 h. The dried extracts were finally resuspended in

25% acetonitrile (ACN) in water containing 0.1% formic acid (FA) for analysis by LC-MS/MS in multiple reaction monitoring (MRM) mode.

Mouse lungs were homogenized using a Precellys/Cryolys Evolution homogenizer from Bertin, France, according to the manufacturer's recommendations using the CK28 ceramic beads 2 mL lysing kit. One hundred milligrams of lung tissue in 400 µL of cold PBS was ground at 4°C for 3 to 6 cycles of 30 s each at 5,000 rpm with a 15 s pause in between each cycle until a smooth homogenate was obtained (3 animals per time point, two independent experiments).

To extract C910 from lung homogenates, samples were washed twice with ice-cold PBS (vortex, centrifugation at 15,000 × g for 10 min, elimination of the supernatant). Then, the pellets were resuspended in DMSO, vortexed and centrifuged twice to extract C910, and both supernatants were combined. A fraction of the DMSO supernatant was diluted with 25% ACN in water containing 0.1% FA and analyzed by LC-MS/MS (MRM mode). The LC-MS/MS system consisted of an Agilent 1100 HPLC coupled online to an Esquire-HCT ion trap mass spectrometer (Bruker-Daltonics) equipped with an electrospray ionization (ESI) source. LC separation was carried out at a flow rate of 200 µL/min with a Thermo Scientific reversed-phase Accucore-150 C18 column (2.1 × 50 mm; 2.6 µm) with a linear gradient of 0–100% B over 7 min with a mobile phase composed of 0.1% FA in water (solvent A) and 0.1% FA in ACN (solvent B). The ESI conditions and detection of C910 and products were optimized, and the IS-spiked samples were quantified. Fragmentation energy amplitudes were also optimized (SmartFrag off). MS detection was performed in MRM mode. The fragmentation transition followed for the dosage of C910 was m/z 337.2 → 125.9. A second fragmentation transition was used to confirm the identity of C910 (m/z 337.2 → 238.0). The fragmentation transitions followed for the internal standard were m/z 436.0 → 284.9 (dosage) and m/z 436.0 → 254.9 (identity confirmation). Data analysis software (Bruker Daltonics) was used for the qualitative and quantitative processing of the raw MS and MS/MS data. The ion chromatograms of the C910 MS/MS transitions as well as of the internal MS standard were extracted as EICs. The EIC peaks were integrated, and the ratio of C910/IS from the corresponding MS transitions enabled us to generate C910 calibration curves in plasma or lung homogenates and further quantify the amount of C910 in these biological matrices from treated mice.

In vivo PK, biodistribution and plasma analysis

Animal care and surgical procedures were performed according to Directive 2010/63/EU of the European Parliament, which had been approved by the Ministry of Agriculture, France. The project was submitted to the French Ethics Committee CEEA (Comité d'Ethique en Expérimentation Animale) and obtained authorization (APAFIS#10108-2017060209348158 v3). Animal protocols in the CIIL (Center for Infection and Immunity of Lille) were approved by the Minister of Higher Education and Research after favorable opinion of the Ethics Committee (CEEA Nord-Pas de Calais n°75/APAFIS#10232-2017061411305485 v6). All experiments were performed in accordance with the relevant named guidelines and regulations. Experiments were conducted on adult male C57BL/6J mice (23.5 ± 0.3 g) purchased from Janvier Labs (Le Genest St Isle, France). Mice were injected intraperitoneally with 10 mg/kg (29,716 nmol/kg) C910. Blood samples were collected at 5 min, 15 min, 30 min, 45 min, 1 h, 6 h and 24 h after injection from three different mice at each time point. Quantification of the C910 concentration contained in the plasma at each time point was performed by LC–MS/MS. PK parameters were calculated from these data with the noncompartmental analysis linear up/log down method using the PKSolver add-in program. Plasmatic toxicology diagnostics were performed 24 h after injection using a Piccolo® AmLyte 13 and the Piccolo Xpress® chemistry analyzer (Abaxis, USA). Levels of glucose, blood urea nitrogen, creatinine, total bilirubin, albumin, alanine aminotransferase, aspartate aminotransferase, creatine kinase, amylase, sodium, potassium, and calcium were determined from the heparinized plasma of five mice injected with DMSO vehicle or C910. Quantitative data are shown as the means, with error bars indicating the standard error of the mean (s.e.m.).

In vivo IAV infection

Viral challenges were carried out on groups of 9∼10-week-old C57BL/6 male mice (Charles River Laboratories). Animals were treated by intraperitoneal injection with either DMSO vehicle or 20 mg/kg C910 as described in the figures. Anesthetized mice were infected intranasally with the IAV H1N1 PR/8 strain (Charles River Laboratories) diluted in 25 µL of PBS at a high dose (1.5×10^5 PFU/mouse, Figures 7A–7C) or low dose (5×10^3 PFU/mouse, Figures S6C and S6D) in the prophylactic setting as well as a dose of 9.5×10^3 PFU/mouse (Figures 7D–7F) in the treatment setting. To minimize suffering, mice were monitored daily for body weight/condition, posture, activity level, grooming and respiratory characteristics. Mice were

euthanized when they showed significant weight loss (greater than 20%) or exhibited signs of immobility or difficulty breathing.

QUANTIFICATION AND STATISTICAL ANALYSIS

All data are presented as the mean ± s.d. or mean ± s.e.m. unless specified in the figure legends. Student's *t* tests were applied to determine statistical significance between two datasets, and one-way ANOVA was used to perform analyses between more than two datasets unless specified in the figure legends. A value of $p \leq 0.05$ was considered significant (denoted *$p \leq 0.05$, **$p < 0.01$, ***$p < 0.001$, ****$p < 0.0001$). GraphPad Prism 6 or 8 software was used to construct the graphs and perform statistical analyses. All statistical details for experiments can be found in the figure legends.